

STUDY OF HIGHER HARMONICS IN THE GRAVITATIONAL WAVE RADIATION OF BINARY BLACK HOLE MERGERS USING PARTICLE SWARM OPTIMIZATION

A dissertation

submitted to the

Indian Institute of Science Education and Research Berhampur

*for the partial fulfilment of BS-MS dual degree in
Physical Sciences*

by

Sweta Sethi

18102



Indian Institute of Science Education and Research, Berhampur

Department of Physical Sciences

April, 2023

Supervisor: Dr. Rajesh Kumble Nayak, IISER Kolkata

© Sweta Sethi, 2023

All rights reserved

DECLARATION

I, **Sweta Sethi (Roll No: 18102)**, hereby declare that, this report entitled **Study of higher harmonics in the gravitational wave radiation of binary black hole mergers using particle swarm optimization**, submitted to Indian Institute of Science Education and Research Berhampur, towards partial requirement of **BS-MS Dual degree** in **Physics**, is an original work carried out by me under the supervision of Dr. Rajesh Kumble Nayak, and has not formed the basis for the award of any degree or diploma, in this or any other institution or university. I have sincerely tried to uphold the academic ethics and honesty. Whenever an external information or statement or result is used then, that have been duly acknowledged and cited.

Berhampur- 760010

Sweta Sethi

April, 2023

CERTIFICATE

This is to certify that the work contained in this dissertation entitled **“Study of higher harmonics in the gravitational wave radiation of binary black hole mergers using particle swarm optimization”** submitted by **Sweta Sethi (Roll No: 18102)** to Indian Institute of Science Education and Research, Berhampur towards the partial requirement of **BS-MS Dual Degree in Physics** has been carried out at Indian Institute of Science Education and Research Kolkata, under the supervision of Dr. Rajesh Kumble Nayak, Professor, Department of Physics, Indian Institute of Science Education and Research Kolkata during the academic year 2022-23.

Dr. Rajesh Kumble Nayak
IISER, Kolkata

Sweta Sethi
IISER, Berhampur

Dedicated to my parents and Swastik.

ACKNOWLEDGEMENT

I would like to express my sincere gratitude to Professor Rajesh Kumble Nayak, IISER Kolkata, for his unwavering support and guidance throughout. His valuable insights, prompt response to my queries, and kind hospitality have been instrumental in my successful completion of the first half of my project.

I am thankful to my loving family which includes my mom, dad and Swastik. Their love, trust and support has been beneficial for the completion of my dissertation. Their generosity and concern has made a significant difference in my life. Without their help, my project would not have moved forward.

I would also like to thank Souradeep Pal, Ph.D. scholar, at IISER Kolkata, for his timely help and support with the coding-related aspects of my project. His expertise and knowledge have been extremely beneficial in resolving the technical difficulties I faced.

I appreciate my friends at CESSI, Yoshita Baruah, Chitradeep Saha, Sakshi Gupta, Souvik Roy, who have helped me to both relax and regain focus.

I am thankful to the CESSI cluster which made the computation faster and simpler. I am obliged to Mr. Prosenjit Lahiri and Mr. Shahid Ali Farooqui for resolving my cluster related issues.

I am also grateful to IISER Kolkata for providing me with the necessary funds throughout the work.

Berhampur- 760010

Sweta Sethi

April, 2023

ABSTRACT

The gravitational wave detector data consist of signals from astrophysical sources and detector noises. The detectors most of the time give a high false alarm rate. False alarm rate is the number of times the system generates an alarm or alert that turns out to be false positive i.e. a situation when the system detects a problem that does not actually exist. For identifying the modeled signal from noise we use a stochastic process which is Particle Swarm Optimization (PSO). In this report, we demonstrate the inclusion of higher modes of gravitational radiation, which emit at the higher multipoles of the orbital frequency than the dominant modes, show significant improvements in the recovery of the parameters of the binary black hole coalescence, as well as the reduction of the false alarm rate using the particle swarm optimization algorithm. Our work focuses on including the higher harmonics in our template and checking the accuracy of the gravitational wave pipeline in the estimation of different parameters of binary black hole coalescence. We also use the transient catalog of binary merger events from the Gravitational Wave Open Science Center (GWOSC) to verify the optimization technique.

Keywords: False alarm rate, Particle Swarm Optimization (PSO), higher harmonics, gravitational wave pipeline

LIST OF ACRONYMS

| | |
|---------------|---|
| GR | General Relativity |
| GW | Gravitational wave |
| GRB | Gamma Ray Burst |
| BBH | Binary Black Hole |
| EM | Electromagnetic |
| CBC | Compact Binary Coalescence |
| BNS | Binary Neutron Star |
| NSBH | Neutron star - Black hole |
| PSD | Power Spectral Density |
| IMR | Inspiral-merger-ringdown |
| Phenom | Phenomenological |
| EOB | Effective-one-body |
| LIGO | Laser Interferometer Gravitational wave Observatory |
| LVC | LIGO-Virgo Collaboration |
| SNR | signal-to-noise |
| PSO | Particle Swarm Optimization |
| FFT | Fast Fourier Transform |
| LVK | LIGO-Virgo-KAGRA Collaboration |
| GWOSC | Gravitational Wave Open Science Center |
| PyCBC | Python for Compact Binary Coalescence |

Contents

List of Figures

| | |
|--|-----------|
| List of Tables | 1 |
| 1 Study of Gravitational waves within the linearised theory of General Relativity | 2 |
| 1.1 Brief overview of General Relativity | 2 |
| 1.2 Gravitational waves | 3 |
| 1.3 Sources of GWs | 8 |
| 2 Detection of Gravitational waves | 10 |
| 2.1 Hulse-Taylor pulsar | 11 |
| 2.2 Ground based interferometric detectors | 12 |
| 2.3 Detector's response | 13 |
| 2.4 Detector noise | 16 |
| 2.5 Gravitational wave data analysis | 17 |
| 3 Particle Swarm Optimization | 22 |
| 3.1 PSO Algorithm | 25 |
| 4 Gravitational waves and spherical harmonics | 28 |

| | | |
|----------|---|-----------|
| 5 | Detecting Gravitational waves containing higher harmonics using PSO | 33 |
| 5.1 | Models and source used | 34 |
| 5.2 | Approach | 34 |
| 5.3 | Results | 37 |
| 5.3.1 | Simulated data | 37 |
| | Results when HM search = True, HM array = [2,2] | 38 |
| | Results when HM search = True, HM array = [2,1], [2,2], [3,3], [4,4] | 39 |
| | Results when HM array = [2,1], [2,2], [3,3], [4,4] and HM search = False | 41 |
| | Results when HM array = [2,1], [2,2], [3,3], [4,4] and HM search = True | 42 |
| 5.3.2 | From Astrophysical source | 44 |
| | Results when HM search = True, HM array = [2,2] | 44 |
| | Results when HM search = True, HM array = [2,1], [2,2], [3,3], [4,4] | 45 |
| 5.3.3 | Chi-squared time-frequency discriminator statistic | 47 |
| 6 | Conclusion and Future Work | 50 |
| | Bibliography | 53 |

List of Figures

| | | |
|-----|---|----|
| 1.1 | A monochromatic gravitational wave of pulsation $\omega = \frac{2\pi}{T}$ propagates along the z direction. The lower panel shows the effects of the purely polarized GWs on a ring of freely falling particles | 8 |
| 1.2 | The spectrum of gravitational waves with sources and detectors. Credit: NIK SPENCER Nature | 9 |
| 2.1 | Hulse and Taylor's observations of binary pulsar PSR B1913+16 orbital decay as a function of time in years. The orbital decay is quantified by the total cumulative amount the binary system has been offset from its first observation in 1975 with respect to the binary's perihelion point (black dots). The solid black curve is representative of the theoretical decay curve predicted by GR. | 12 |
| 2.2 | An illustration of LIGO detectors. The detectors use a laser to emit photons which pass through a beam splitter and travel down two arms of the detectors. The photons then hit test mass mirrors and are caught in a Fabry-Perot signal recycling cavity which increases their sensitivity. After reflecting back and forth in the Fabry-Perot cavities, photons are released and return to the beam splitter, recombining and being recorded on a set of photodiodes which measure the phase difference between photons from both arms. This information is encoded in the interference pattern on the readout of the detector photodiodes, which is the final output of the detectors. | 14 |

| | | |
|-----|---|----|
| 2.3 | The antenna pattern of an interferometric detector with the arms in the x-y plane and oriented along the two axes. The response F for waves coming from a certain direction is proportional to the distance to the point on the antenna pattern in that direction. | 15 |
| 2.4 | Lower frequencies are largely dominated by seismic motion, mid-range frequencies are dominated by thermal coating Brownian motion on the mirrors as well as quantum vacuum noise between 10 and 100 Hz and higher frequencies are dominated by quantum vacuum shot noise. | 17 |
| 2.5 | Strain data for the frame file from the detector | 18 |
| 2.6 | Flowchart shows the steps that PyCBC uses to find the signal and measure their significance. | 19 |
| 2.7 | Power spectral density plot | 21 |
| 3.1 | Search space | 23 |
| 3.3 | Representation of the Particle Swarm Optimization (PSO) model | 25 |
| 3.4 | Particle Swarm Optimization algorithm schema | 26 |
| 4.1 | Plot shows the angle used in this study | 30 |
| 4.2 | Violin plots for the posteriors of the intrinsic parameters (chirp mass(M_c), mass ratio(q), M_{total} , and χ_{eff}) when injected with IMRPhenomHM and recovered using IMRPhenomHM and IMRPhenomD model at mass ratio $q=2$ (blue), 4(gray), 8(orange) at an inclination of 0^0 , 60^0 and 90^0 . Opacity represents the likelihood values. | 31 |
| 4.3 | Recovery of $\theta_{[jn]}$ for IMRPhenomHM injection at inclination 0^0 , 60^0 and 90^0 and IMRPhenomD as the recovery waveform models. The left, center, and right columns depict the inclination recovery for the $q = 2, 4$, and 8 configurations, respectively, with the recovery for each inclination laid out by horizontal dashed-black lines. Black, blue, and red dotted lines represent the actual injection values at 0 degrees, 60 degrees, and 90 degrees, respectively. | 32 |

| | | |
|------|---|----|
| 5.1 | We demonstrate how various modes appear in the detector band. The plot illustrates the real part of the whitened modes of a compact binary coalescence waveform over time. We have used only those modes h_{lm} which are available IMRPhenomHM. We notice higher the value of m , the earlier it enters the frequency band of the detector. Also, we notice non-zero amplitudes of higher modes before the merger happens. | 36 |
| 5.2 | When HM search = True, HM array = [2,2] | 39 |
| 5.3 | When HM search = True, HM array = [2,1], [2,2], [3,3], [4,4] | 40 |
| 5.4 | When HM array = [2,1], [2,2], [3,3], [4,4] and HM search = False | 42 |
| 5.5 | When HM array = [2,1], [2,2], [3,3], [4,4] and HM search = True | 43 |
| 5.6 | When HM search = True, HM array = [2,2] | 45 |
| 5.7 | When HM search = True, HM array = [2,1], [2,2], [3,3], [4,4] | 46 |
| 5.8 | Output files for (A) Simulated event and (B) Real event | 47 |
| 5.9 | SNR Time Series plot which contains one signal and two glitches | 48 |
| 5.10 | Re-weighted SNR time series plot, where the SNR peaks at signal | 49 |

List of Tables

| | | |
|-----|---|----|
| 5.1 | Parameters in search space | 34 |
| 5.2 | Injection parameters in different search categories | 35 |

Chapter 1

Study of Gravitational waves within the linearised theory of General Relativity

1.1 Brief overview of General Relativity

Einstein proposed the general theory of relativity in 1915 in response to a flaw in Newton's theory of gravity. According to Newton's theory, the gravitational force propagates instantaneously, meaning that any changes in mass distribution would result in changes everywhere in the universe immediately. This conflicts with Einstein's special theory of relativity, which states that information cannot travel faster than the speed of light [1]. Therefore, Einstein developed a new theory of gravity to address this issue.

Einstein used the principle of equivalence to develop the mathematical formulation of the general theory of relativity. This principle states that reference frames with a uniform gravitational field, like the Earth, are equivalent to frames that are accelerating with respect to an inertial reference frame, like a freely falling elevator. This led to the prediction that gravitational fields should bend the path of photons, which was confirmed by Eddington in 1919 when he showed that light from distant stars bent due to the gravitational field of the sun [2]. The general theory of relativity has been extensively tested over the years and has consistently agreed with experimental results. It has also been used to make predictions, such as the existence of gravitational waves, which were confirmed by LIGO in 2016 [3]. This theory has had a significant impact on modern physics and cosmology. It predicts that gravity arises as a consequence of the interaction between the geometry of spacetime and its

matter-energy content. The relationship is expressed in the form of Einstein's field equations ¹:

$$G_{\alpha\beta} = 8\pi T_{\alpha\beta} \quad (1.1)$$

where $G_{\alpha\beta}$ represents the geometry or curvature of the spacetime through the Einstein tensor i.e.

$$G_{\alpha\beta} = R_{\alpha\beta} - \frac{1}{2}g_{\alpha\beta}R \quad (1.2)$$

where $R_{\alpha\beta}$ is the Ricci tensor, R is the Ricci scalar and $g_{\alpha\beta}$ is the metric tensor.

The right hand side of Eq.1.1 through the stress-energy tensor $T_{\alpha\beta}$ represents the matter-energy content of the universe [4]. The indices α, β run over four spacetime indices taking values 0,1,2,3. In this dynamical relationship, matter and spacetime are entangled together, which is best expressed through John Wheeler's famous words: "Spacetime tells matter how to move; matter tells spacetime how to curve"

1.2 Gravitational waves

In the weak gravitational field or in the absence of gravity, the spacetime is considered flat with small perturbation $h_{\mu\nu}$ and is characterised by the Minkowski tensor $\eta_{\mu\nu}$, and $g_{\mu\nu}$ being the correction over the metric for flat Minkowskian spacetime $\eta_{\mu\nu}$

$$g_{\mu\nu} = \eta_{\mu\nu} + h_{\mu\nu} \quad (1.3)$$

where

$$|h_{\mu\nu}| \ll 1 \quad (1.4)$$

¹Unless stated explicitly in the thesis, we will be using the geometrized units for which the Newton's constant and the velocity of light are set to unity, i.e. $G = c = 1$

and the flat Minkowski metric η in the cartesian coordinate, which is the matrix is given as:

$$\eta_{\mu\nu} = \begin{bmatrix} +1 & 0 & 0 & 0 \\ 0 & -1 & 0 & 0 \\ 0 & 0 & -1 & 0 \\ 0 & 0 & 0 & -1 \end{bmatrix} \quad (1.5)$$

We will see that gravitational waves (linearized gravity) are the disturbances in the $h_{\mu\nu}$ terms.

The inverse spacetime metric is defined as

$$g^{\mu\nu} = \eta^{\mu\nu} - h^{\mu\nu}, |h^{\mu\nu}| \ll 1 \quad (1.6)$$

where

$$h^{\mu\nu} = h_{\rho\sigma} \eta^{\rho\mu} \eta^{\sigma\nu} \quad (1.7)$$

Since, $\partial_\rho g_{\mu\nu} = \partial_\rho h_{\mu\nu}$, we replace it in the connection coefficient formula to get,

$$\Gamma_{\mu\nu}^\sigma = \frac{1}{2} g^{\sigma\nu} (\partial_\nu h_{\alpha\mu} + \partial_\mu h_{\alpha\nu} - \partial_\alpha h_{\mu\nu}) \quad (1.8)$$

$$= \frac{1}{2} (\eta^{\sigma\nu} - h^{\sigma\nu}) (\partial_\nu h_{\alpha\mu} + \partial_\mu h_{\alpha\nu} - \partial_\alpha h_{\mu\nu}) \quad (1.9)$$

According to linearized gravity, both $|h^{\sigma\alpha}| \ll 1$ and $|\partial_\mu h_{\mu\nu}| \ll 1$, so product is also small.

Thus we get

$$\Gamma_{\mu\nu}^\sigma = \frac{1}{2} \eta^{\sigma\nu} (\partial_\nu h_{\alpha\mu} + \partial_\mu h_{\alpha\nu} - \partial_\alpha h_{\mu\nu}) \quad (1.10)$$

We then calculate the Riemann tensor in linearized gravity,

$$R_{\sigma\mu\nu}^\rho = \partial_\mu (\Gamma_{\nu\sigma}^\rho) - \partial_\nu (\Gamma_{\mu\sigma}^\rho) + \Gamma_{\nu\sigma}^\gamma \Gamma_{\mu\gamma}^\rho - \Gamma_{\mu\sigma}^\delta \Gamma_{\nu\delta}^\rho \quad (1.11)$$

Using Eq.1.10 in Eq.1.11, we get the Riemann tensor as

$$R_{\sigma\mu\nu}^\rho = \frac{1}{2} \eta^{\rho\alpha} (\partial_\mu \partial_\sigma h_{\nu\alpha} - \partial_\mu \partial_\alpha h_{\nu\sigma} - \partial_\nu \partial_\sigma h_{\mu\alpha} + \partial_\nu \partial_\alpha h_{\mu\sigma}) \quad (1.12)$$

Next we calculate the Ricci tensor which is just the Riemann tensor with its upper and lower middle indices summed together i.e.

$$R_{\sigma\nu} = R_{\sigma\mu\nu}^{\mu} \quad (1.13)$$

From Eq.1.12 we get,

$$R_{\sigma\mu\nu}^{\mu} = \frac{1}{2}\eta^{\mu\alpha}(\partial_{\mu}\partial_{\sigma}h_{\nu\alpha} - \partial_{\mu}\partial_{\alpha}h_{\nu\sigma} - \partial_{\nu}\partial_{\sigma}h_{\mu\alpha} + \partial_{\nu}\partial_{\alpha}h_{\mu\sigma}) \quad (1.14)$$

Thus the linearized Ricci tensor is given as,

$$R_{\sigma\nu} = \frac{1}{2}(\partial_{\mu}\partial_{\sigma}h_{\nu}^{\mu} + \partial_{\nu}\partial_{\alpha}h_{\sigma}^{\alpha} - \partial_{\nu}\partial_{\sigma}h - \square h_{\nu\sigma}) \quad (1.15)$$

where, \square is the d'Alembertian operator which is given as

$$\square \equiv \eta^{\mu\alpha}\partial_{\mu}\partial_{\alpha} = \partial_{\mu}\partial^{\mu}$$

and

$$h \equiv h_{\mu}^{\mu} = \eta^{\mu\alpha}h_{\mu\alpha}$$

We then calculate the Ricci scalar in the linearized gravity, which is

$$R = R_{\nu}^{\nu} = \eta^{\sigma\nu}R_{\sigma\nu} \quad (1.16)$$

Using Eq.1.15 in Eq.1.16 and η to raise all the ν indices to become σ , we get

$$R = \partial_{\mu}\partial_{\sigma}h^{\mu\sigma} - \square h \quad (1.17)$$

So, Ricci scalar in linearized gravity is the second partial derivative of h with raised indices minus the d'Alembertian of the h -scalar. Since we found out the Ricci tensor, Ricci scalar in linearized gravity, Eq.1.2 can now be rewritten as

$$G_{\mu\nu} = \frac{1}{2}(\partial_{\alpha}\partial_{\mu}h_{\nu}^{\alpha} + \partial_{\alpha}\partial_{\nu}h_{\mu}^{\alpha} - \square h_{\mu\nu} - \partial_{\mu}\partial_{\nu}h) - \frac{1}{2}\eta_{\mu\nu}(\partial_{\alpha}\partial_{\beta}h^{\alpha\beta} - \square h) \quad (1.18)$$

$$= \frac{1}{2}(\partial^\alpha \partial_\mu h_{\nu\alpha} + \partial^\alpha \partial_\nu h_{\mu\alpha} - \square h_{\mu\nu} - \partial_\mu \partial_\nu h - \eta_{\mu\nu} \partial^\alpha \partial^\beta h_{\alpha\beta} + \eta_{\mu\nu} \square h) \quad (1.19)$$

We introduce a new component \bar{h} as below, also called trace-reverse tensor of $h_{\mu\nu}$ and replace it with all the h-components in Eq.1.19

$$\bar{h}_{\mu\nu} \equiv h_{\mu\nu} - \frac{1}{2}\eta_{\mu\nu}h \implies h_{\mu\nu} = \bar{h}_{\mu\nu} + \frac{1}{2}\eta_{\mu\nu}h \quad (1.20)$$

Thus,

$$G_{\mu\nu} = \frac{1}{2} \left[\partial^\alpha \partial_\mu \bar{h}_{\nu\alpha} + \partial^\alpha \partial_\nu \bar{h}_{\mu\alpha} - \partial^\alpha \partial_\alpha \bar{h}_{\mu\nu} - \eta_{\mu\nu} \partial^\alpha \partial^\beta \bar{h}_{\alpha\beta} \right] \quad (1.21)$$

So we can write the Einstein field equation by linearized gravity as

$$G_{\mu\nu} = \frac{1}{2} \left[\partial^\alpha \partial_\mu \bar{h}_{\nu\alpha} + \partial^\alpha \partial_\nu \bar{h}_{\mu\alpha} - \partial^\alpha \partial_\alpha \bar{h}_{\mu\nu} - \eta_{\mu\nu} \partial^\alpha \partial^\beta \bar{h}_{\alpha\beta} \right] = \frac{8\pi G}{c^4} T_{\mu\nu} \quad (1.22)$$

Given the Einstein's field equation for linearized gravity, it is possible to do a change of coordinates where all terms go to zero except $\partial^\alpha \partial_\alpha \bar{h}_{\mu\nu} = \square \bar{h}_{\mu\nu}$. It turns out that if we can find out a coordinate system where $\partial_\beta \bar{h}^{\alpha\beta} = 0$, which is the Lorenz-gauge condition, then the first three terms of Eq.1.22 goes to zero, and we have

$$G_{\mu\nu} = \frac{1}{2}(-\partial^\alpha \partial_\alpha \bar{h}_{\mu\nu}) = \frac{8\pi G}{c^4} T_{\mu\nu} \quad (1.23)$$

In vacuum, where $T_{\mu\nu} = 0$, the weak field equation becomes,

$$\partial^\alpha \partial_\alpha \bar{h}_{\mu\nu} \equiv \square \bar{h}_{\mu\nu} = 0 \quad (1.24)$$

This directly shows that the metric perturbation \bar{h} is a solution to the wave equation. From Eq.1.24 we can write the d'Alembertian as the second derivative of our spacetime coordinate,

$$\frac{\partial^2 \bar{h}_{\mu\nu}}{\partial (ct)^2} - \frac{\partial^2 \bar{h}_{\mu\nu}}{\partial x^2} - \frac{\partial^2 \bar{h}_{\mu\nu}}{\partial y^2} - \frac{\partial^2 \bar{h}_{\mu\nu}}{\partial z^2} = 0 \quad (1.25)$$

and rewrite the spatial derivatives as the Laplacian operator,

$$\frac{1}{c^2} \frac{\partial^2 \bar{h}_{\mu\nu}}{\partial t^2} = \nabla^2 \bar{h}_{\mu\nu} \quad (1.26)$$

This is the wave equation in three dimensions. Therefore Einstein field equation predicts

existence of waves that can travel through the curvature of spacetime in the form of small perturbations away from flat metric.

The wave equation in three-dimensions as in Eq.1.26 has a plane-wave solution as:

$$\bar{h}_{\mu\nu} = A_{\mu\nu} e^{ik_\sigma x^\sigma} \quad (1.27)$$

where the amplitude $A_{\mu\nu}$ is propagating with wave vector k_σ . Using the Lorenz gauge condition on the solution we get $A_{\mu\nu}$ is orthogonal to the wave propagation vector k i.e.

$$k_\beta A^{\alpha\beta} = 0 \quad (1.28)$$

Next we pick up a specific Lorenz gauge coordinate system called the *transverse-traceless* (TT) gauge by defining four constraints in the wave amplitude $A_{\mu\nu}$. Three being the transverse constraints which come from requiring that the wave oscillations are transverse to an observer with a four-velocity U ,

$$A_{\mu\nu} U^\mu = 0 \quad (1.29)$$

and

$$A^\mu_\mu = 0 \quad (1.30)$$

which demands that A is traceless.

The amplitude $A_{\mu\nu}$ has 16 components, out of which 6 are redundant due to the inherent symmetry of $h_{\mu\nu}$, 8 components are redundant because they are a result from our freedom to choose whatever coordinate system we like in spacetime i.e. if we focus on the Lorenz gauge class of coordinate system and further narrow down to unique TT gauge coordinate system, we see that only two independent components A_{xx} and A_{xy} that corresponds to gravitational wave polarization (for a wave propagating in z-direction),

$$A_{\mu\nu} = \begin{bmatrix} 0 & 0 & 0 & 0 \\ 0 & A_{xx} & A_{xy} & 0 \\ 0 & A_{xy} & -A_{xx} & 0 \\ 0 & 0 & 0 & 0 \end{bmatrix} \quad (1.31)$$

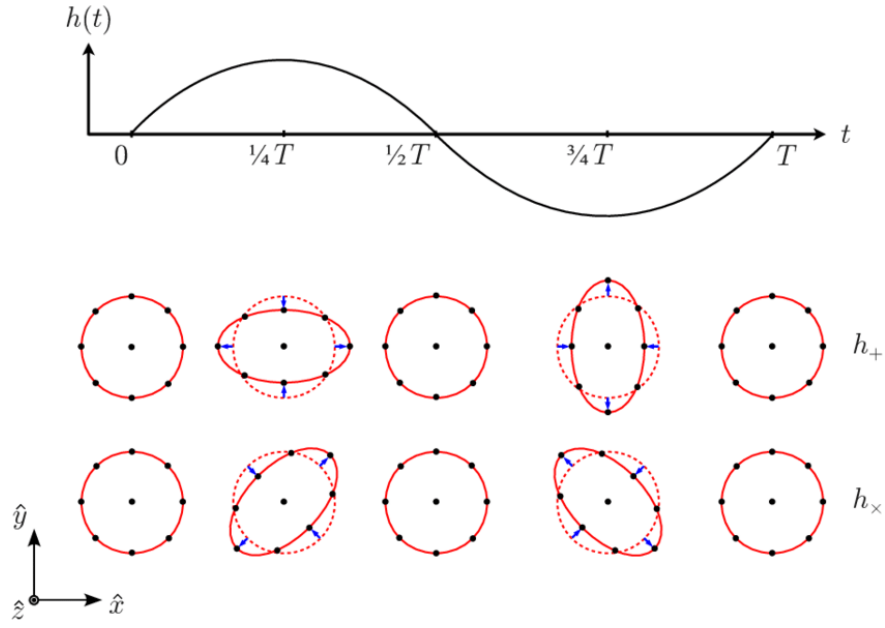


FIGURE 1.1: A monochromatic gravitational wave of pulsation $\omega = \frac{2\pi}{T}$ propagates along the z direction. The lower panel shows the effects of the purely polarized GWs on a ring of freely falling particles

The concept of interferometry to detect GWs came from Fig. 1.1, where Kip Thorne, Ronald Drever, and Rainer Weiss put forward the idea that the movement of mirrors of Michelson interferometer could lead to the detection of GWs.

1.3 Sources of GWs

There are many astrophysical and cosmological sources of gravitational waves, which can be categorized as follows:

1. **Inspiral:** An inspiral gravitational wave source is a binary system in which two objects, such as binary black holes (BH-BH) or binary neutron stars (NS-NS), or neutron star-black hole (NS-BH) orbit each other and gradually spiral inward due to the emission of gravitational waves. As they spiral closer together, the frequency and amplitude of the emitted gravitational waves increase until the objects eventually merge.
2. **Continuous:** A continuous gravitational wave source is a source of gravitational waves that emits waves at a constant frequency over a long period of time. This is in contrast

to inspiral sources, which emit gravitational waves at varying frequencies as the objects spiral towards each other. Continuous gravitational wave sources can include a wide range of objects like pulsars, rapidly rotating neutron stars, supernova remnants, spinning black holes, cosmic strings.

3. Burst: Burst gravitational waves are short-lived and transient signals that can be produced from supernova or gamma ray burst.
4. Stochastic: A stochastic background of gravitational waves can be created by the early universe, similar to the Cosmic Microwave Background (CMB), but originating from a younger epoch, just after the Big Bang..

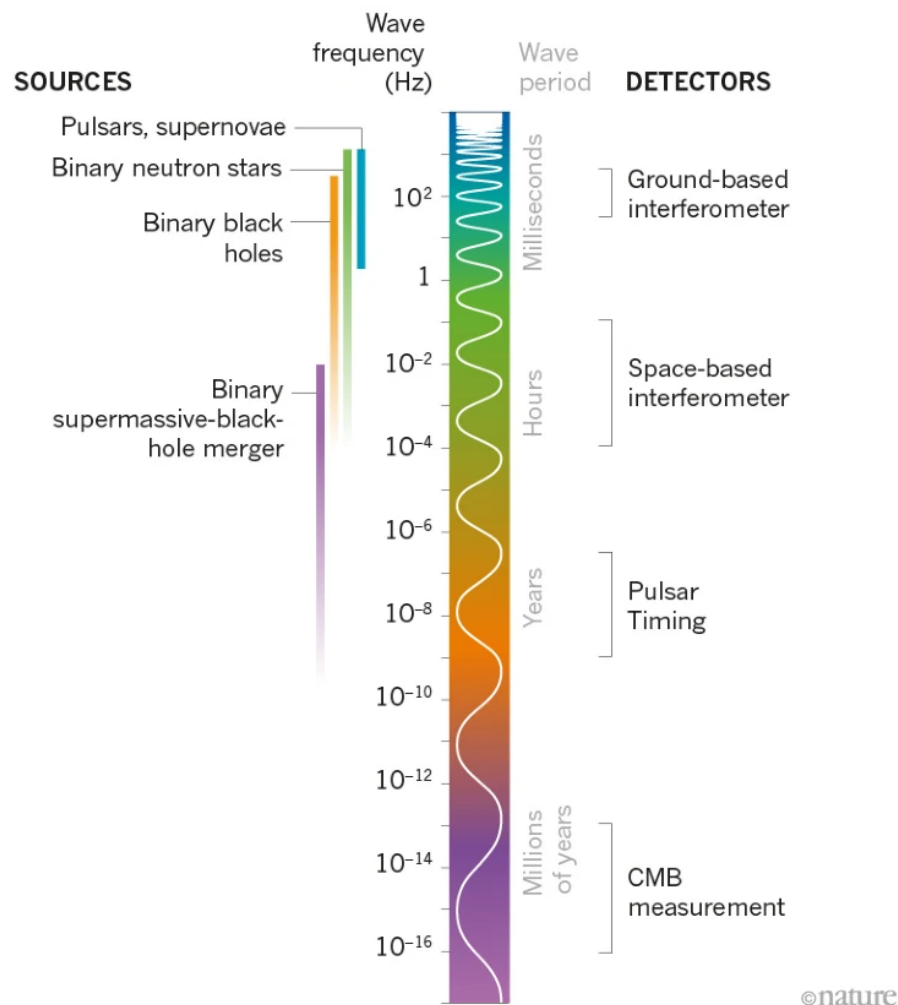


FIGURE 1.2: The spectrum of gravitational waves with sources and detectors.
Credit: NIK SPENCER Nature

Chapter 2

Detection of Gravitational waves

The Laser Interferometer Gravitational-Wave Observatory (LIGO), Virgo and KAGRA Collaboration (LVK) has carried out several observation runs since its inception. The initial operations ran from 2002 to 2010, but no gravitational waves (GWs) were detected during this period. During the first observing run in the advanced detector era (September 2015 - January 2016), the LVK detected a total of 3 binary black hole (BBH) mergers, including GW150914 [3], GW151226 [5], and GW151012 [6]. GW150914 was the first detected BBH with a signal-to-noise ratio (SNR) value of approximately 25.1 [7]. GW151012 was initially labeled as a less significant potential GW detection (LVT151012) due to its high false alarm rate but was later upgraded to a confirmed GW event in the GWTC-1 catalogue because its false alarm rate was less than 1 per 30 days, a threshold determined by the LVC [8]. The change in false alarm rate for GW151012 can be attributed to various improvements made to all search algorithms used in the first observation run between the initial detection and publication of the GWTC-1 catalogue paper.

During the second observing run (November 2016 - August 2017), the LVK detected an additional 7 BBHs with total masses between approximately 18.6M and 85.1M. The second observation run saw the first detection of a binary neutron star (BNS) event GW170817. The BNS event had the highest network SNR of any event over all of O1 and O2, approximately 32.4. Approximately 1.7 seconds following GW170817, a gamma-ray burst (GRB) (GRB170817) was observed across multiple wavelengths of the electromagnetic (EM) spectrum over several weeks [9].

During the first half of the third observing run (April 2019 - March 2020), the LVK collaboration made an additional 39 confirmed GW event detections [6, 8]. The increase in the number of detections can be attributed to higher sensitivities of the detectors during this observation run over previous runs, with a BNS range of 108Mpc, 135Mpc, and 45Mpc for Hanford, Livingston, and Virgo, respectively.

In January 2020, the LVK collaboration reported the first detection of two NSBH events (GW200105 and GW200115) [10]. The primary component masses of both events are approximately $8.9M_{\odot}$ and $5.7M_{\odot}$, respectively, whose mass values are both above the maximum allowed mass of a neutron star (NS), so may therefore be likely classified as black hole (BH)s. The secondary masses of each event were given as approximately $1.5M_{\odot}$ and $1.9M_{\odot}$, respectively, and were reported to be within the range of known NSs [11].

Overall, the progress made by the LVK collaboration in the detection and analysis of GW events has opened up new avenues for understanding the Universe, and it is expected that even more groundbreaking discoveries will be made in the coming years as the detectors continue to improve.

2.1 Hulse-Taylor pulsar

The search for gravitational waves began as early as 1970. The first indirect evidence was made by Russell Alan Hulse and Joseph Hooton Taylor Jr., for their observation of orbital decay or loss of energy to the gravitational radiation of binary pulsars, also known as Hulse-Taylor pulsar [12]. Their observation matched the decay that was predicted by Einstein's theory of relativity as shown in Fig. 2.1[13].

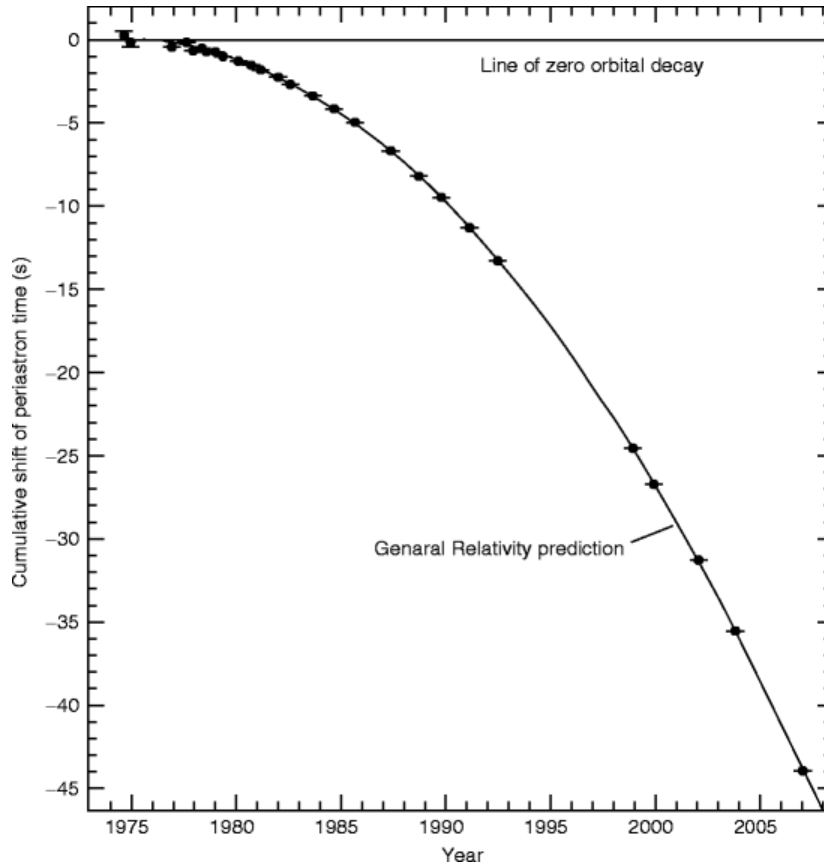


FIGURE 2.1: Hulse and Taylor’s observations of binary pulsar PSR B1913+16 orbital decay as a function of time in years. The orbital decay is quantified by the total cumulative amount the binary system has been offset from it’s first observation in 1975 with respect to the binary’s perihelion point (black dots). The solid black curve is representative of the theoretical decay curve predicted by GR.

2.2 Ground based interferometric detectors

The current generation of ground-based gravitational wave (GW) detectors in the Laser Interferometer Gravitational-Wave Observatory (LIGO) Scientific Collaboration (LVC) consist of three observatories: two in North America, located in Hanford, Washington State and Livingston [14], Louisiana, and one in Pisa, Italy, known as Virgo [15]. There are also other ground-based detectors in Hannover, Germany (GEO) [16] and Kamioka, Japan (KAGRA) [17]. In addition to these detectors, there are plans to build space-based observatories, such as the Laser Interferometer Space Antenna (LISA) [18] and TianQin [19], which will search

for supermassive binary black holes (BBHs) and other sources.

Each detector, except for LISA and TianQin, can be thought of as a large-scale Michelson-Morley interferometer [20] composed of two arms perpendicular to each other. Each arm of the LIGO detectors is 4 km long, while the Virgo arms are slightly shorter at 3 km. A simplified schematic of an interferometric GW detector is shown in Fig. 2.2.

In the schematic, a laser emits a 1064nm laser beam that passes through a phase modulator (PMOD) and enters the power recycling cavity (PRM). The PRM boosts the signal's power. The beam then passes through a beam splitter (BS), which divides the laser beam path into two parts. Each part travels through an input test mass and hits end test masses at the end of both interferometer arms. The beams are then caught in a Fabry-Perot cavity [21], which extends the distance traveled by the laser light photons and their power. This cavity stores the photons for approximately 1 ms, allowing a potential GW signal more time to interact with the photons, thereby increasing the sensitivity of the interferometer at low frequencies.

Some laser light escapes back down both arms and recombines at the BS, where the recombined beam passes through a signal recycling mirror (SRM). Finally, the beam hits a set of photodiodes (PD) that produce the interferometer readout. The readout is a measure of the phase difference between photons from both arms, which is encoded in the interference pattern on the readout of the detector photodiodes. This pattern is the final output of the detectors.

2.3 Detector's response

It is also to be noted that the sensitivity of the detectors may be influenced by the orientation of the detectors with respect to the source of GWs. The sensitivity of the LVC detectors

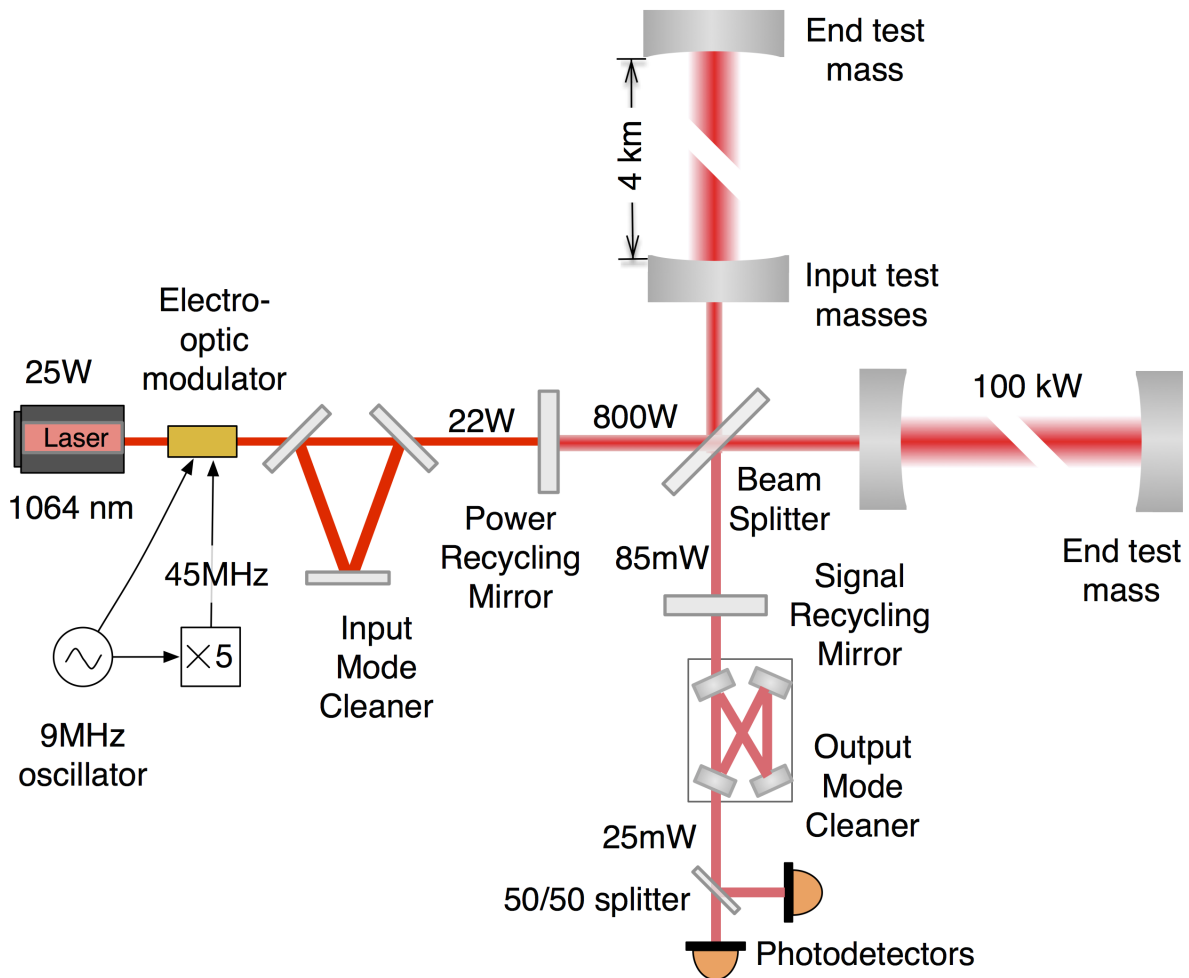


FIGURE 2.2: An illustration of LIGO detectors. The detectors use a laser to emit photons which pass through a beam splitter and travel down two arms of the detectors. The photons then hit test mass mirrors and are caught in a Fabry-Perot signal recycling cavity which increases their sensitivity. After reflecting back and forth in the Fabry-Perot cavities, photons are released and return to the beam splitter, recombining and being recorded on a set of photodiodes which measure the phase difference between photons from both arms. This information is encoded in the interference pattern on the readout of the detector photodiodes, which is the final output of the detectors.

is not uniform across all parts of the sky. This non-uniformity is characterized by the detectors' antenna patterns, which mathematically describe how sensitive they are to different directions and polarizations of gravitational waves (GWs) depending on the source location relative to the detector. These antenna patterns have a significant impact on the strain measurements made by the LVC detectors, as they affect the signal-to-noise ratio of the detected GW signals. The accuracy and precision of GW measurements are therefore dependent on the knowledge and understanding of the detectors' antenna patterns.

The detector response can be expressed as [22],

$$F_+ = -\frac{1}{2}(1 + \cos^2 \theta) \cos 2\phi \cos 2\psi - \cos \theta \sin 2\phi \sin 2\psi \quad (2.1)$$

$$F_x = +\frac{1}{2}(1 + \cos^2 \theta) \cos 2\phi \sin 2\psi - \cos \theta \sin 2\phi \cos 2\psi \quad (2.2)$$

where F_+ and F_x are called the antenna pattern function of the detector, expressed in terms of the sky position of the source. θ is the azimuthal angle, ϕ is the polar angle, both with respect to the reference frame fixed at the center of Earth. ψ is the polarization angle which is counter-clockwise around the direction of GW propagation \mathbf{d} is the angle from the line of nodes to the x-axis of the GW source reference frame. θ , ϕ , ψ are the Euler angles which describe the frame of the binary system with respect to the detector.

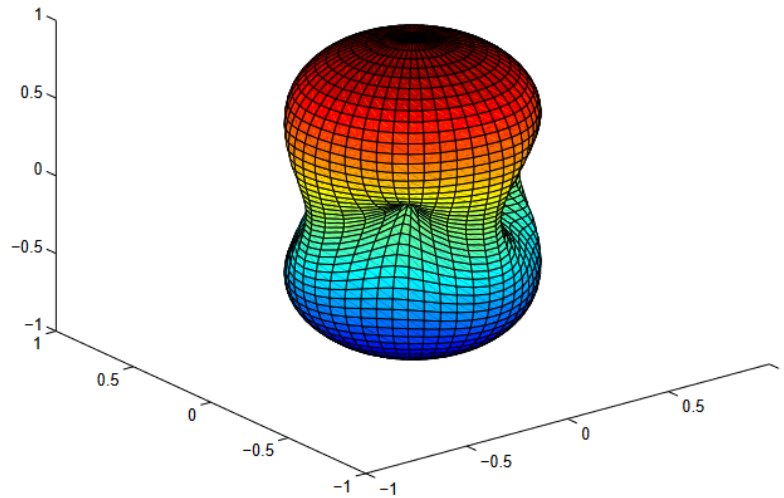


FIGURE 2.3: The antenna pattern of an interferometric detector with the arms in the x-y plane and oriented along the two axes. The response F for waves coming from a certain direction is proportional to the distance to the point on the antenna pattern in that direction.

When a gravitational wave (GW) passes through a detector, it causes the detector to respond to a linear combination of the two independent polarizations of the wave, which is dependent on the orientation of the detector and the direction of the source. As a result, no single detector can directly measure both polarizations of the GW simultaneously. However, if the GW signal is short-lived, the response of three detectors with widely separated locations, along with the time differences between their detections, can be used to reconstruct the source location and polarization. For a long-lived GW signal, the location of the source within the detector's antenna pattern changes as the detector moves, causing frequency modulation of the signal. These effects can also be used to determine the location of the source and polarization of the GW. In summary, the geometry of the detector and its response to GWs allow for the reconstruction of the source location and polarization, which is a critical component of understanding the properties and origins of GW sources.

2.4 Detector noise

The LVC detectors are also susceptible to a variety of non-astrophysical sources of noise as shown in Fig. 2.4. These noise sources can produce signals that mimic GW signals and can limit the detectors' sensitivity by creating periods of excess power in the measured data. There are several common sources of noise that the LVC detectors must contend with, including gravity-gradient noise, seismic noise, thermal noise, and quantum shot noise. Gravity-gradient noise arises from variations in the local gravitational field, while seismic noise results from ground vibrations caused by natural phenomena such as earthquakes or human activity such as nearby construction. Thermal noise is caused by the thermal motion of the atoms in the detector material, while quantum shot noise arises from the discrete nature of electromagnetic radiation. Mitigating the impact of these noise sources is an ongoing challenge for the LVC collaboration, and significant efforts are made to understand and reduce them through advanced techniques such as active vibration isolation, thermal stabilization, and signal processing algorithms.

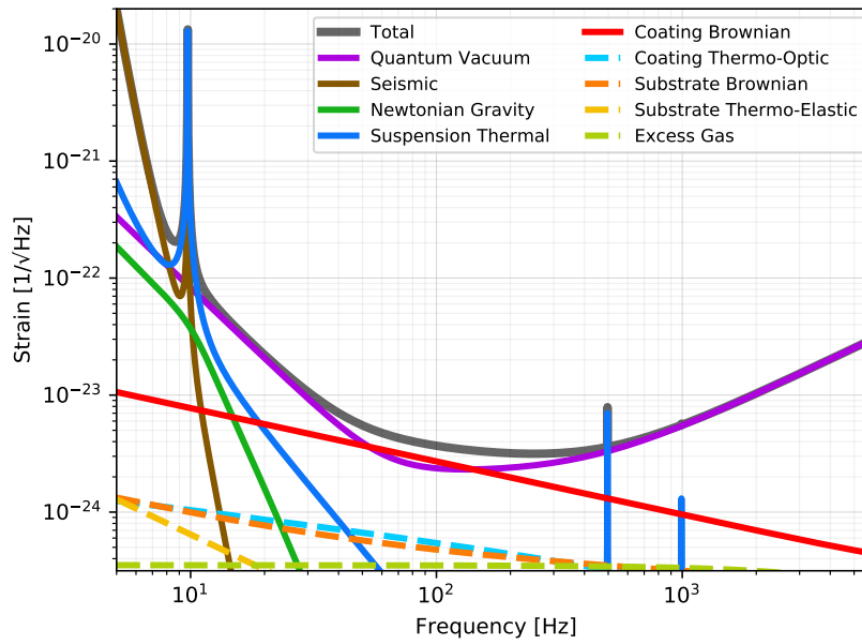


FIGURE 2.4: Lower frequencies are largely dominated by seismic motion, mid-range frequencies are dominated by thermal coating Brownian motion on the mirrors as well as quantum vacuum noise between 10 and 100 Hz and higher frequencies are dominated by quantum vacuum shot noise.

2.5 Gravitational wave data analysis

Search pipelines are an essential tool in gravitational wave astronomy for the identification of the gravitational-wave candidates from the detector data. The Python Compact Binary Coalescence (PyCBC) search pipeline is a widely used pipeline for detecting gravitational waves from compact binary coalescences (CBCs) which include binary black holes and binary neutron stars [23, 24]. The PyCBC pipeline is designed to be computationally efficient, scalable, and userfriendly. One of the key features of using the PyCBC pipeline is that it is written in Python and it is the ability to perform coherent searches across multiple detectors. Coherent searches involve obtaining data from multiple detectors and improving the sensitivity and accuracy of the search.

The aim of the PyCBC pipeline is to identify candidate gravitational-wave signals from the binary coalescences in the detector data and provide a measure of their statistical significance. To detect these signals sophisticated signal processing techniques are required as the amplitude of most gravitational wave sources is comparable to the noise background. Fig.2.6

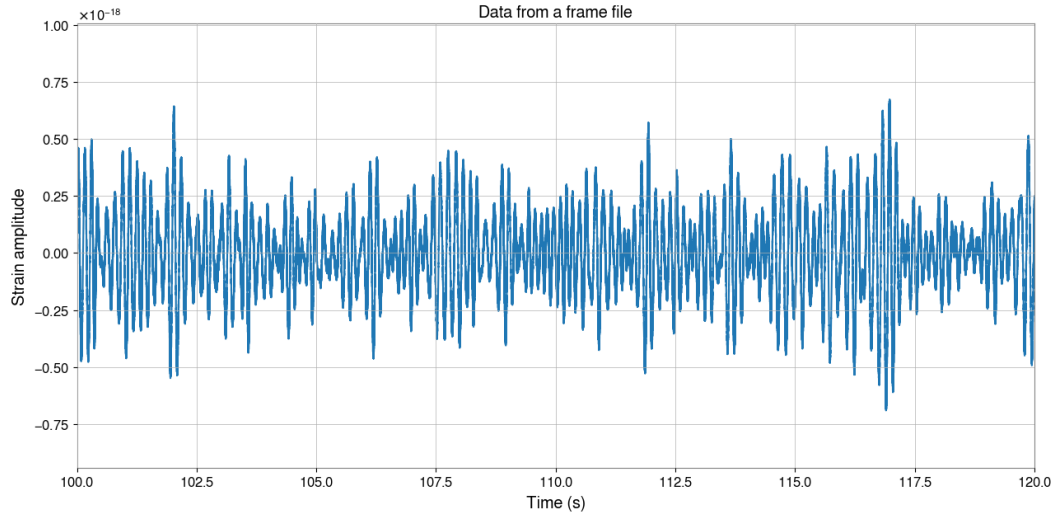


FIGURE 2.5: Strain data for the frame file from the detector

shows the steps the pipeline follows for finding and measuring the significance of signals. The input to the pipeline is the calibrated strain data from the detector which consists of gaussian and non-gaussian noise components. Data quality investigations are done independently of the search pipelines and by only at looking the detector's performance, thus data suitable for astrophysical searches are only taken into consideration.

The signal from the gravitational wave is weak and can be easily buried in the noise of the detector. To identify a gravitational wave signal we need to compare the data to a large number of theoretical waveforms or templates, which are generated by numerical simulations of the black hole or neutron star mergers. Each template represents a possible gravitational wave signal that we might expect to see in the data. This is done using a matched filtering technique, which involves correlating the data with the template waveform to maximize the signal-to-noise ratio. The template that produces the highest correlation is identified as the best match to the data and can be used to extract information about the source of the gravitational wave.

In the Newtonian approximation, the GW signal is computed as [25, 26]:

$$h(t) = A(t) \cos[\psi(t) + \psi_0], \quad t \geq t_0 \quad (2.3)$$

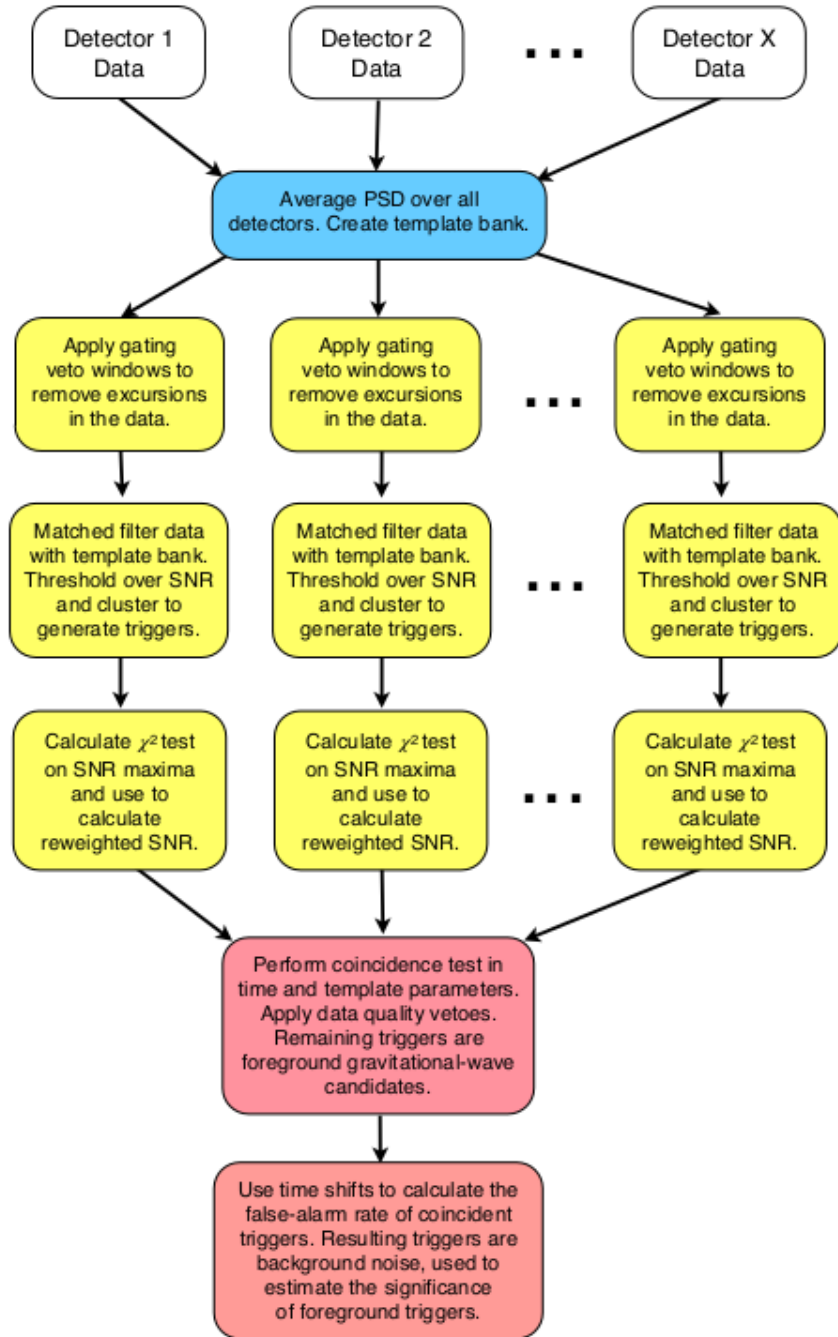


FIGURE 2.6: Flowchart shows the steps that PyCBC uses to find the signal and measure their significance.

where A_t is the amplitude which is given as:

$$A(t) = \mathcal{G} \frac{4\mathcal{M}^{5/3} \pi^{2/3} F(t)^{2/3}}{D} \quad (2.4)$$

where \mathcal{M} is the chirp mass ($\mathcal{M} = \frac{(m_1 m_2)^{3/5}}{(m_1 + m_2)^{1/5}}$), D is the luminosity distance to the source, $F(t)$ is the instantaneous frequency of the GW, and \mathcal{G} depends on the sky-location of the source and its orientation concerning the detector. Again, $\psi(t)$ in Eq.1 is the GW signal phase, which is given as:

$$\psi(t) = \psi_0 + 2\pi \int_0^{t-t_0} F(t') dt' \quad (2.5)$$

ψ_0 in Eq.1 is the GW phase when the signal reaches the detector at $t=t_0$ and $F=F_0$, where F_0 is the lowest frequency at which the detector operates. The instantaneous frequency of the GW, $F(t)$ as in Eq.2 depends on source parameters that are given as:

$$F(t) = F_0 \left(1 - \frac{t-t_0}{T_c} \right)^{-3/8} \quad (2.6)$$

where, T_c is the chirp duration expressed as:

$$T_c = \frac{5}{256(\pi F_0)^{8/3} \mathcal{M}^{5/3}} \quad (2.7)$$

The detector data can be modeled as an addition of the signal $h(t)$ and random noise $n(t)$, and it can be written as:

$$x(t) = h(t) + n(t) \quad (2.8)$$

The signal $h(t)$ is buried under the stationary gaussian noise, and we use matched filtering for the signal extraction. It works by comparing a pre-determined waveform, known as a template waveform, to the data collected by the detector. The template waveform is adjusted to match the data by altering its parameters, and a correlation is calculated between the two. The correlation function for two time series $x(t)$ and $\tilde{h}(t)$ for a time shift τ is defined as:

$$R(\tau) = \int_{-\infty}^{\infty} x(t) \tilde{h}^*(t - \tau) dt \quad (2.9)$$

To detect signal buried in the Gaussian white noise, we have

$$R(\tau) = \int_{-\infty}^{\infty} \tilde{x}(f) \tilde{h}^*(f) e^{i2\pi f \tau} df \quad (2.10)$$

When the noise is colored, the frequency spectrum of the noise is not flat but has variation in powers across different frequencies. These are characterized by power spectral density (PSD). The corresponding matched filter output is given as:

$$R(\tau) = 4 \int_0^{\infty} \frac{\tilde{x}(f) \tilde{h}^*(f)}{S(f)} e^{i2\pi f \tau} df. \quad (2.11)$$

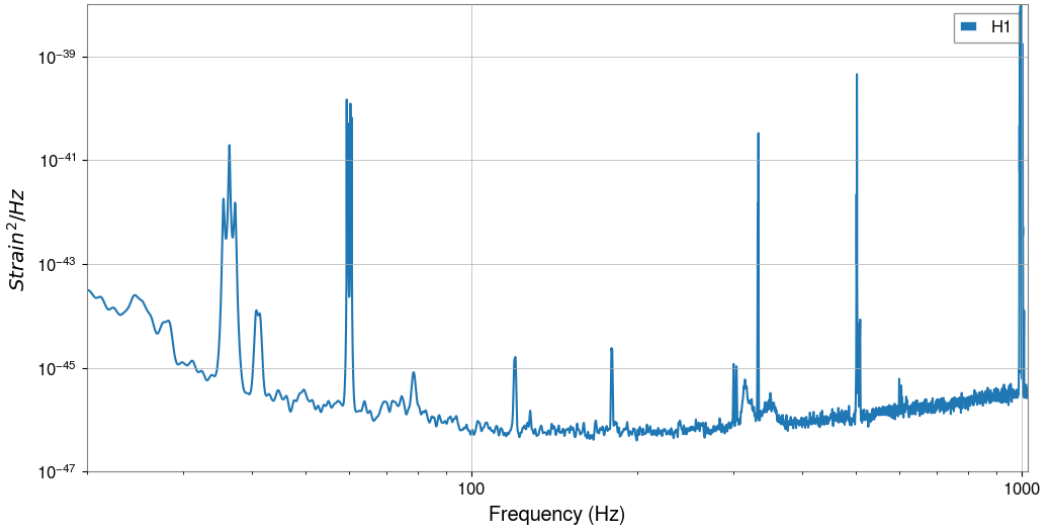


FIGURE 2.7: Power spectral density plot

The correlation function $R(\tau)$ is then squared and integrated to get the signal-to-noise ratio (SNR). The result is a scalar value that represents the strength of the GW signal relative to the noise. The higher the SNR, the more likely it is that the signal is genuine and not just noise.

$$SNR^2 = 4 \int_0^{\infty} \frac{|\tilde{h}(f)|^2}{S(f)} df. \quad (2.12)$$

Chapter 3

Particle Swarm Optimization

Particle Swarm Optimization (PSO) is a heuristic optimization algorithm developed by Dr. James Kennedy and Dr. Russell Eberhart, who were researchers at the Department of Computer Science and Electrical Engineering at the University of Kentucky in 1995 [27]. They were inspired by the social and dynamic movements of birds, fish, and insects that move in groups or flocks or schools where they communicate and follow each other or their leaders in search of food or a new home. In PSO, a group of particles (also called agents or individuals) moves through the search space. Each particle adjusts its movement based on its own experience (*pbest*) and the experience of other particles in the group (*gbest*), resulting in a swarm-like behavior in the search space, and finding a good solution to the optimization problem.

In PSO, the **pbest** and the **gbest** are the two important concepts that influence the movement of particles in the search space. The *pbest* of the particle is the best position that the particle has found so far in the search space. It is initialized to the initial position of the particle and updated whenever the particle finds the best solution. It guides the particle's movement and encourages exploring a new area of the search space that may contain a better solution. However, the *gbest* is the best position that any particle in the group has found so far. It is initialized to the personal best of the first particle and updated whenever any particle finds a better solution. The *gbest* guides the movement of all the particles in the search space and ensures they are moving toward the best solution found so far. Thus in PSO, the movement of particles is a combination of its *pbest* and *gbest*, with a velocity that is updated with each iteration in the algorithm, based on the current position and the previous velocity

of the particle. Because of this update in the velocity, the particles later converge toward a good solution.

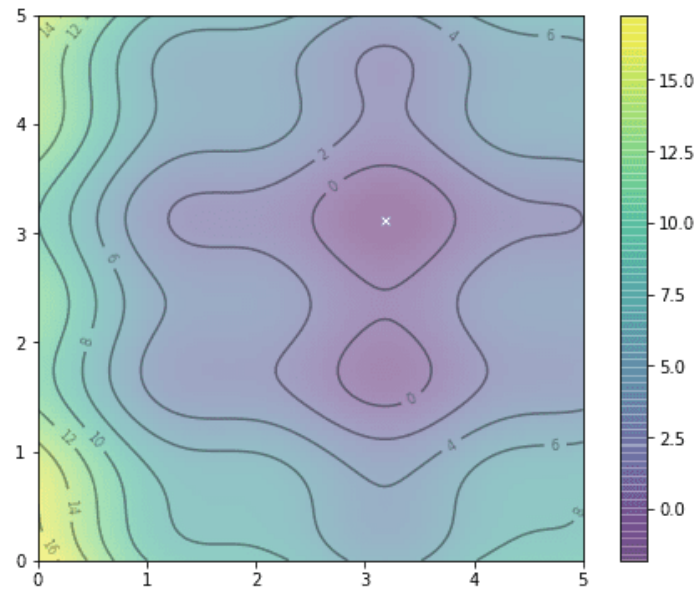
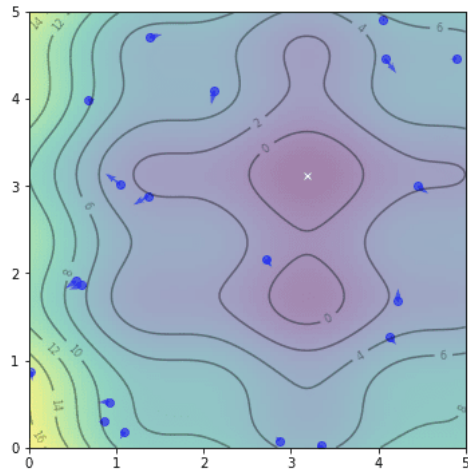
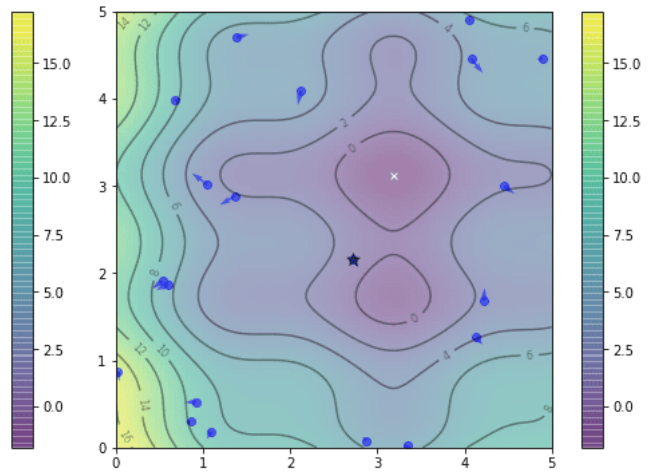


FIGURE 3.1: Search space

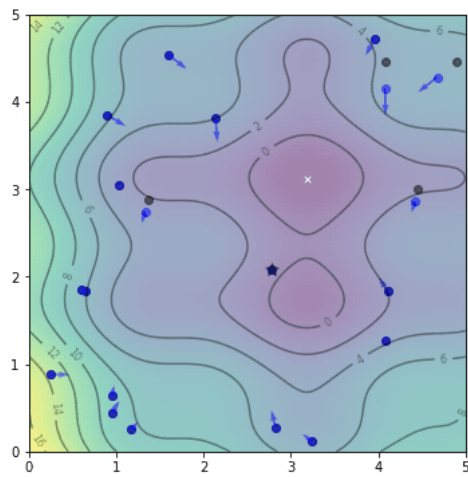
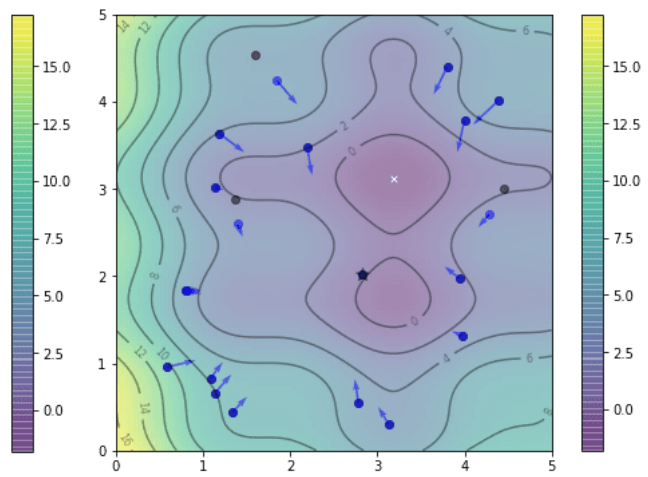
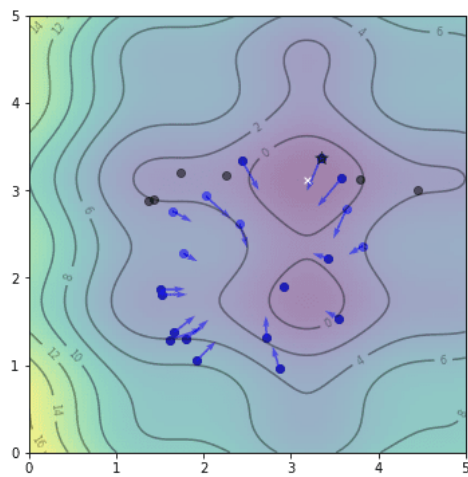
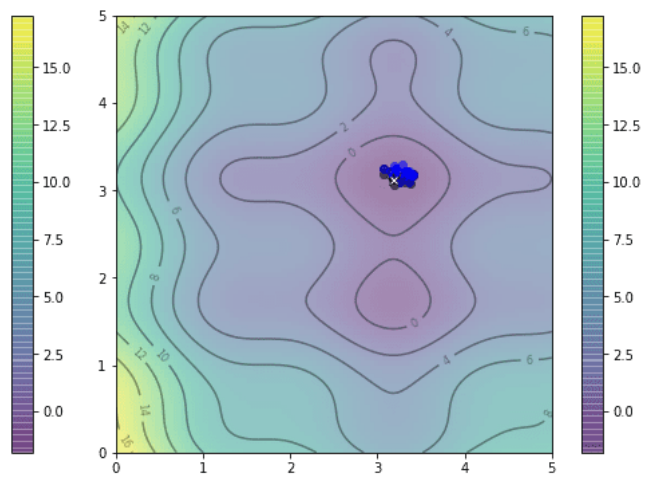
PSO is a metaheuristic algorithm that can be applied to a wide range of optimization problems, like in engineering, finance, and biology, and to solve optimization problems such as finding the maximum or minimum of a function (objective function), minimizing the cost of a process, or optimizing the parameters of a system. It has been used in combination with other techniques, such as neural networks or genetic algorithms, to solve complex problems. However, the choice of parameters like inertial weight, acceleration constants, and population size can affect the algorithm's performance.



(A) Initial position of particles



(B) gbest is marked as a star

(C) 1st iteration(D) 2nd iteration(E) 5th iteration(F) 20th iteration

3.1 PSO Algorithm

The representation of the PSO model is shown in Fig. 3.1 [28]. The X and Y represent the horizontal and the vertical search space respectively.

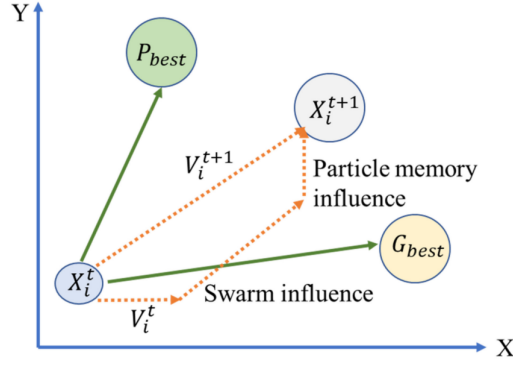


FIGURE 3.3: Representation of the Particle Swarm Optimization (PSO) model

Each particle is composed of 3 vectors:

1. X-vector: It records the current position (location) of a particle in search space.
2. P-vector: Personal best or *pbest*. It records the location of the best solution found so far by the particle.
3. V-vector: It contains the gradient (direction) for which the particle will travel if it is undisturbed.

The equation governing the position and velocity is given as,

$$X_{t+1} = X_t + V_{t+1} \quad (3.1)$$

which is also called the updated position as shown in the flowchart in Fig.3.4. X_t is the current position.

The updated velocity is given as,

$$V_{t+1} = \omega \dot{V}_t + c_1 \text{random}(0, 1)(pbest - X_t) + c_2 \text{random}(0, 1)(gbest - X_t) \quad (3.2)$$

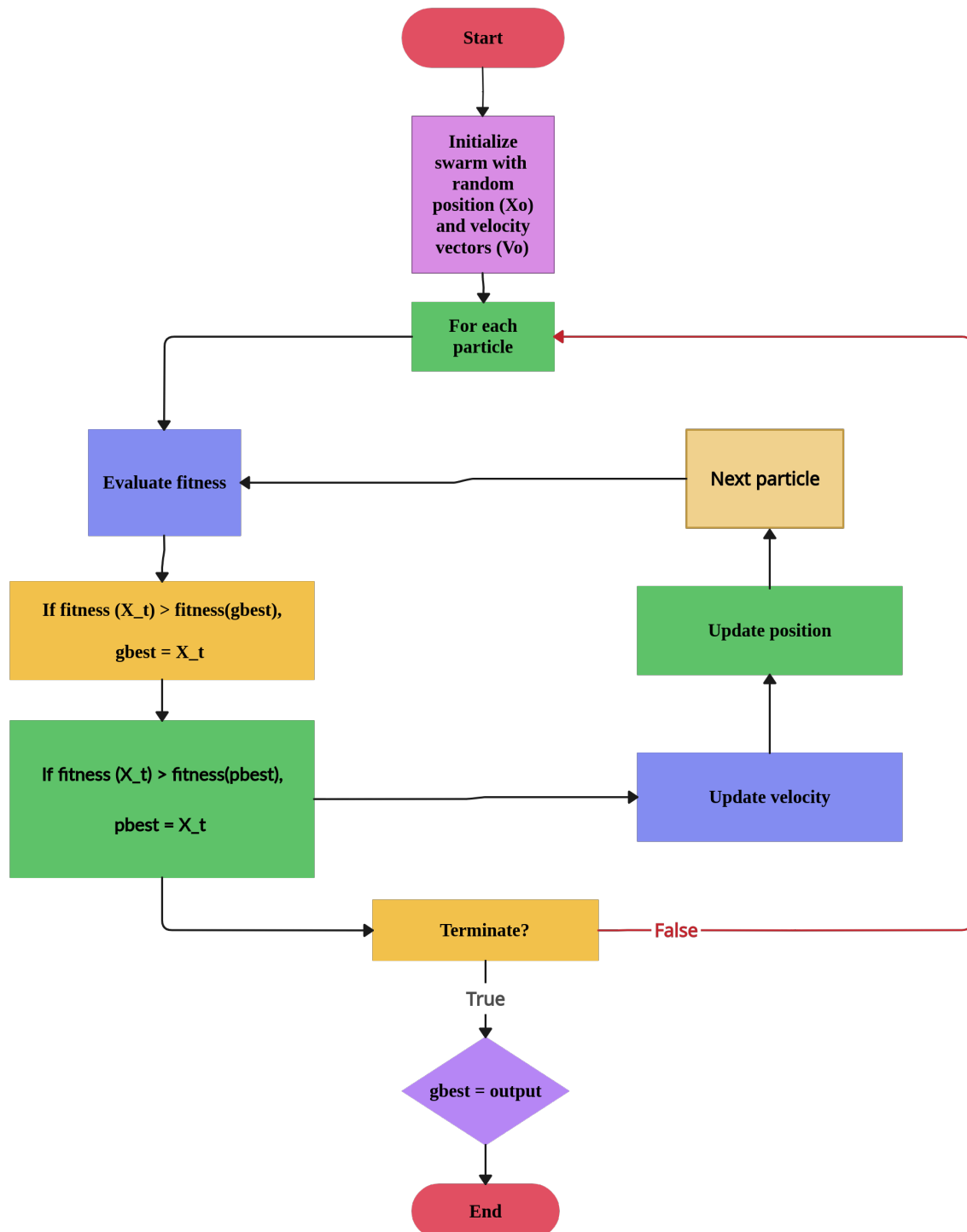


FIGURE 3.4: Particle Swarm Optimization algorithm schema

where V_t is the current position, c_1 and c_2 are the acceleration coefficient and ω is the inertial weight. Larger ω leads to a greater global search ability. The acceleration coefficient determines the inclination of the search. When the first acceleration coefficient exceeds the second, it leads to a greater global search ability. Similarly, when the second leads the first acceleration coefficient, we get a greater local search ability.

PSO has several advantages over traditional optimization algorithms including, it is simple to implement and does not require the use of derivatives or other complex mathematical concepts. It is fast and efficient and can find good solutions to problems. It can also handle continuous, discrete, and mixed-variable optimization problems.

PSO has been applied to a wide range of optimization problems including machine learning problems like neural network training and hyperparameter optimization, in genetic engineering, to solve continuous optimization problems, such as function optimization and gradient-based optimization. PSO is sensitive to the choice of hyperparameters like the size of the swarm and the acceleration coefficient.

Chapter 4

Gravitational waves and spherical harmonics

Spherical harmonics were first developed by mathematician Pierre-Simon Laplace in the late 18th century as a way to solve certain partial differential equations that arise in the study of spherical objects. They were later used by physicists to describe the behavior of waves on the surface of a sphere, such as sound waves or electromagnetic waves. In the 20th century, they were also applied to the study of gravitational waves. Spherical harmonics are a set of functions that are defined on the surface of a sphere and are used to decompose a function defined on the sphere into a series of modes, each of which corresponds to a different pattern of oscillation. By expressing the gravitational wave in terms of spherical harmonics, it is possible to study the different modes of the wave separately and understand how they contribute to the overall shape of the wave.

$$Y_l^m(\theta, \phi) = (-1)^m \left[\frac{(2l+1)(l-m)!}{4\pi(l+m)!} \right]^{1/2} P_l^m(\cos\theta) \exp(im\phi) \quad (4.1)$$

where θ and ϕ are the polar and azimuthal angles respectively, and $P_l^m(x)$ is the associated Legendre polynomial.

Gravitational waves from compact binary coalescence, such as black holes or neutron stars, can be broken down into different types of wave patterns, called spherical harmonic multipoles.

$$h(t, \theta, \phi) = 4\pi \sum_{l=2}^{\infty} \sum_{m=-l}^l h_l^m(t) Y_l^m(\theta, \phi) \quad (4.2)$$

where $h(t, \theta, \phi)$ is the gravitational wave strain at the point (t, θ, ϕ) on the sky. $Y_{lm}(\theta, \phi)$ are the spherical harmonics, l is the degree, m is the order, and h_{lm} are the spherical harmonics coefficient, which are complex numbers that encode the strength and phase of each multipole [29].

The most prominent of these is the quadrupole mode, which is generated by the acceleration of the objects' quadrupole moments. The quadrupole moment is the most important emission mode for gravitational waves, but for more complex systems, other multipole moments can become important as well. The octupole moment is related to the distribution of mass in a system that is traceless and symmetric. When such a system emits gravitational waves, it does so in the form of a superposition of different multipole moments, where each multipole is associated with a different frequency and phase. The octupole moment is associated with the octupole mode, which is a subdominant mode of gravitational wave emission. Octupole mode is an example of how the subdominant mode of emission can carry additional information about the source of the gravitational waves and can be used to improve our understanding of the physical processes that generated the waves. For example, the octupole mode can carry information about the spin of compact objects, and the parameters of their orbits. The detection of such subdominant modes is challenging. This is because the amplitude of the wave is much smaller than the dominant quadrupole mode and it requires advanced data analysis techniques and high-sensitivity detectors to detect it. These subdominant modes become increasingly important as the objects' mass ratio becomes more unequal or as the angle of the collision becomes more inclined about the detector. Not taking these modes into account can cause inaccuracies in measurements.

Gravitational wave signal can be decomposed into the spherical harmonics multi-poles which consists of the dominant and the sub-dominant modes. The dominant modes, also known as the quadruple mode is represented as $(l, |m|) = (2, 2)$. However, it has been found the contribution of sub-dominant mode gives accurate recovery of the different intrinsic and extrinsic parameters of binary mergers [30]. The waveform models describing the inspiral, merger, and ringdown (IMR) stages of the compact binary mergers can be of non-spinning, aligned spin or precessing configuration. We have used the aligned spin model i.e. IMRPhenomHM [30], which is a computationally expensive higher mode phenomenological waveform approximant.

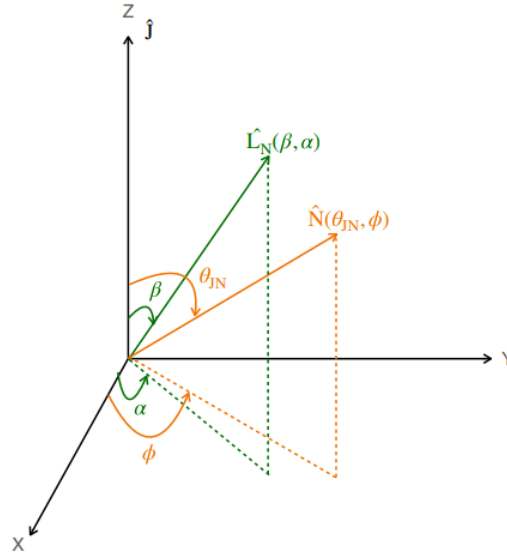


FIGURE 4.1: Plot shows the angle used in this study

The use of higher mode waveforms came into use after the first detection of gravitational waves from GW170729 [31], which was a result of two unequal binaries, which proposed the use of higher mode (or sub-dominant mode) waveform model to recover the parameters accurately.

The gravitational wave signal is a fifteen dimensional function and consists of eight intrinsic parameters (mass and spin) and rest of the extrinsic parameters (luminosity distance, inclination angle, sky location, geocent time, RA, DEC) [?]. For a system when the binary's inclination to the detector changes from face-on ($\theta = 0^0$) to edge-on ($\theta = 90^0$), the role of the dominant mode decreases and that of the sub-dominant mode increases. The recoveries by IMRPhenomHM are not only better constrained but also they break the luminosity distance and the inclination angle degeneracy [30].

In Fig.4.2, we see the bimodal behaviour of IMRPhenomD at $q=8$ and $\theta_{IN} = 90^0$. This is due to the effects of the priors over the parameters and the inaccuracy of the waveform model to create a true-multi mode signal. Even IMRPhenomHM shows bi-modality, but the priors are better constrained.

In Fig.4.3, the recovery of the extrinsic parameters i.e. inclination angle and the luminosity distance, it is found that by using the dominant mode at a higher inclination, the distance

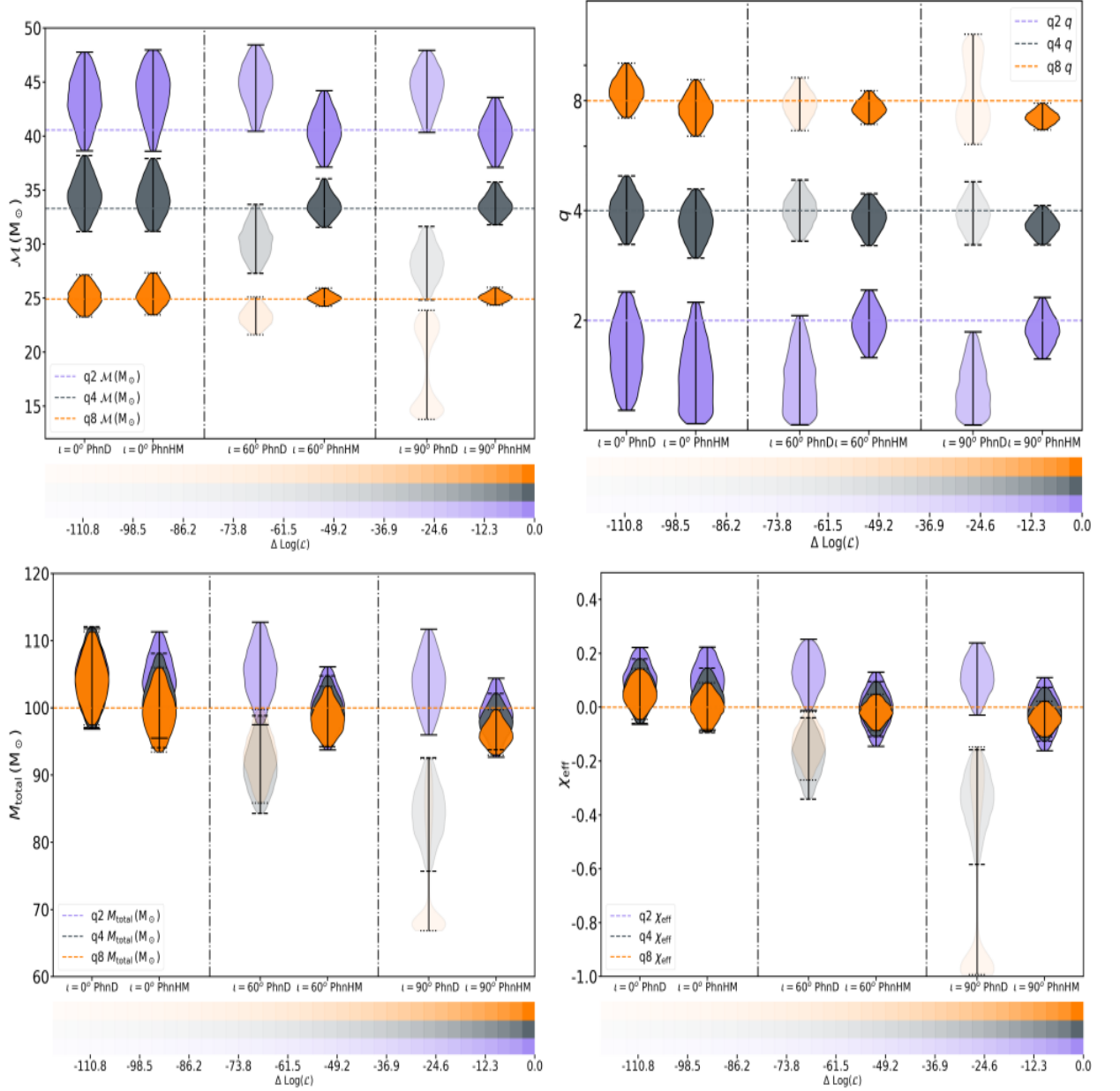


FIGURE 4.2: Violin plots for the posteriors of the intrinsic parameters (chirp mass(M_c), mass ratio(q), M_{total} , and χ_{eff}) when injected with IMRPhenomHM and recovered using IMRPhenomHM and IMRPhenomD model at mass ratio $q=2$ (blue), 4(gray), 8(orange) at an inclination of 0° , 60° and 90° . Opacity represents the likelihood values.

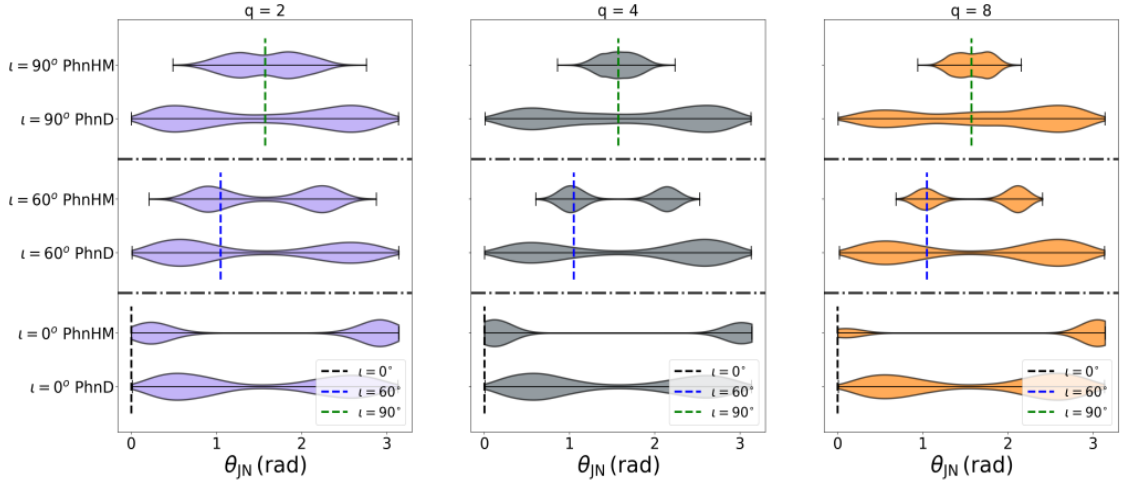


FIGURE 4.3: Recovery of $\theta_{[jn]}$ for IMRPhenomHM injection at inclination 0° , 60° and 90° and IMRPhenomD as the recovery waveform models. The left, center, and right columns depict the inclination recovery for the $q = 2$, 4 , and 8 configurations, respectively, with the recovery for each inclination laid out by horizontal dashed-black lines. Black, blue, and red dotted lines represent the actual injection values at 0 degrees, 60 degrees, and 90 degrees, respectively.

gets overestimated because the recovered inclination angle has more support from the non-edge inclination, and it also shows a bimodal behavior. Thus a multi-mode template can contain the degeneracy between the inclination, polarization, and phase thus leading to an improved value of inclination and better precession of luminosity distance. For IMRPhenomHM injection at inclination of 60° and 90° , the recovered inclination peaks up at true value. Because the systematic errors in the IMRPhenomHM model are almost completely introduced into the higher multipoles, the edge-on systems will exhibit the largest systematic errors because this is where the higher multipoles contribute the most to the signal. However, the bias only manifests itself in instances where the two objects are edge-on to one another. Due to the fact that edge-on systems are still approximately half as powerful as equivalent face-on systems, it is eight times less likely for them to be detected.

Chapter 5

Detecting Gravitational waves containing higher harmonics using PSO

Particle Swarm Optimization is a highly effective algorithm in for finding optimal solutions in higher-dimensional spaces [32, 33]. An astrophysical black hole is characterised by its mass and dimensionless spin vector. The gravitational waveform from a black hole binary is characterised by fifteen parameters such as mass, spin, luminosity distance, phase etc. Recovering astrophysical signals from a noisy data stream and estimating the parameters of the astrophysical source is a computationally expensive task. Our project aims to use PSO to reduce the computational burden involved in extracting signals from noise. Reducing the cost of computation would lead to a shorter time to recover the signal, and we could have a faster prompt system to notify observatory collaborations worldwide to start looking for electromagnetic (EM) counterparts of GW events. In our project, we are also interested in estimating the parameters of the astrophysical source with considerable accuracy during the detection process. This is crucial, as EM counterparts from BH-BH mergers or extreme mass ratio NS-BH binaries are unlikely. If initial estimates are precise, then the observatory will save important time resources.

In this chapter, we discuss which gravitational waveform approximant to use when looking for the subdominant modes in the gravitational wave radiation. We will describe the different parameters used for recovering the GW signal using PSO. First, we include higher harmonics in our machine language and check the accuracy of the gravitational wave pipeline in the estimation of different parameters of binary black hole coalescence using different kinds of

permutation and combination with PSO. Second, to check the efficiency of PSO, we implemented our source code on two real merger events from Gravitational Wave Open Science Center (GWOSC) [34].

5.1 Models and source used

| Compact objects | Primary mass (M_1) | Secondary mass (M_2) |
|-----------------|------------------------|--------------------------|
| BNS | 1 to 3 | 1 to 3 |
| NSBH | 5 to 10 | 1 to 3 |
| BBH1 | 5 to 20 | 5 to 20 |
| BBH2 | 20 to 60 | 5 to 20 |
| BBH3 | 20 to 60 | 20 to 60 |
| BBH4 | 60 to 80 | 60 to 80 |

TABLE 5.1: Parameters in search space

In this work, we perform parameter estimation for the binary black hole mergers of $20\text{-}60M_\odot$ with the standard waveform approximant to the outgoing radiation of coalescing binary black hole; phenomenological time-domain inspiral and merger models, specifically using IMRPhenomHM for the aligned spin black hole system. Fig. 5.1 shows the various modes present in IMRPhenomHM and their appearance in the detector band.

5.2 Approach

Our aim is to develop PSO algorithm to detect higher harmonics [35, 36, 37] in the GW signals buried in noise. We test if the algorithm helps us to recover different parameters of the binary coalescence with great efficiency and accuracy. The injection parameters are grouped and summarized in table 5.2 We simulate the algorithm for 1000 injections containing a

| Injection mode | Injection and recovery | Parameters used | |
|---|--|----------------------|----------------|
| Injection mode = 2 : Signal with noise | HM search = True HM array = [2,2] | Mass m_1 | 10-100 |
| | | Mass m_2 | 10-100 |
| | HM search = True HM array = [2,1], [2,2], [3,3], [4,4] | Spin S_{1z} | -0.5 to 0.5 |
| | | Spin S_{2z} | -0.5 to 0.5 |
| | HM array = [2,1], [2,2], [3,3], [4,4] | Lower frequency | 20 |
| | HM search = True | Higher frequency | 1000 |
| | HM array = [2,1], [2,2], [3,3], [4,4] | Number of swarms | 1 |
| | HM search = False | Number of particles | 1000 |
| Injection mode = 4 : Real signal (O3b) with noise | HM search = True HM array = [2,2] | Detector | LIGO — Hanford |
| | HM search = True HM array = [2,1], [2,2], [3,3], [4,4] | Waveform approximant | IMRPhenomHM |

TABLE 5.2: Injection parameters in different search categories

total of 1000 particles in a single swarm in a two-dimensional space (aligned spin) with eccentricity and spin disabled, to save the computational cost. We added the search for higher modes in the detection. We first add injections which have no GW signal, but only stationary gaussian noise. The reason for adding and searching over a time-series of noise is that any detection algorithm should not claim or trigger or generate a false alarm when there is just noise in the data stream. , and to each injection, we add white noise weighed using the Power Spectral Density (PSD) of the LIGO detectors. Thus we have simulated the data output from the GW detectors which have a signal buried inside the noise. The next step is to be able to detect the signal using the PSO algorithm. First, our work uses only simulated data, and then we work on astrophysical source events which includes the binary black hole mergers in the third observing run of the Advanced LIGO-Virgo. All the injections and the results are obtained using PyCBC, a python based GW data analysis pipeline.

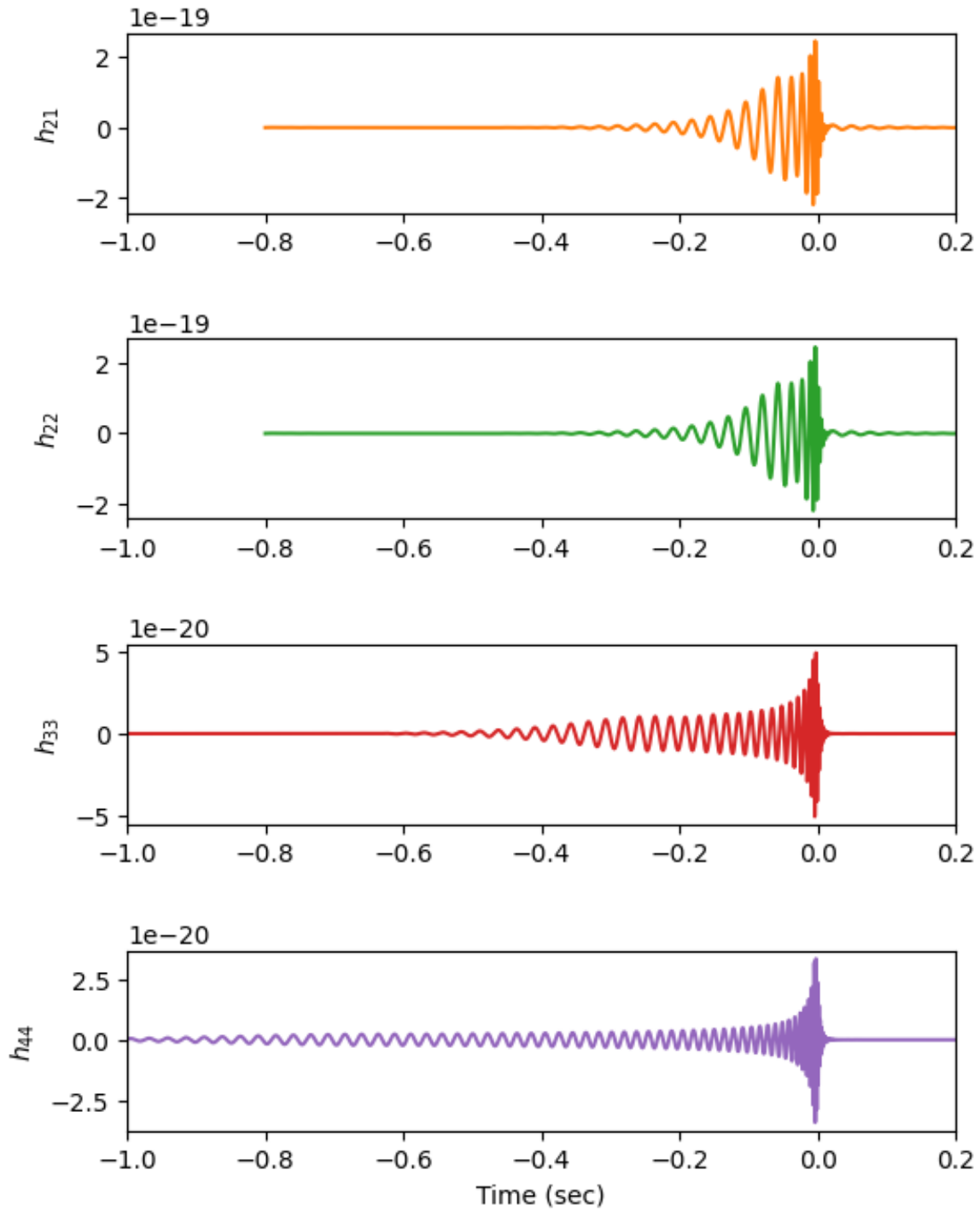


FIGURE 5.1: We demonstrate how various modes appear in the detector band. The plot illustrates the real part of the whitened modes of a compact binary coalescence waveform over time. We have used only those modes h_{lm} which are available IMRPhenomHM. We notice higher the value of m , the earlier it enters the frequency band of the detector. Also, we notice non-zero amplitudes of higher modes before the merger happens.

5.3 Results

We had three sets of observations: one when looking for higher modes ($HM_{search} = True$) in the signals and recovering it with higher modes ($HM_{array} = True$), second when not searching for the higher modes ($HM_{search} = False$) in the signal and recovering using higher modes ($HM_{array} = True$), third injecting a signal with higher modes ($HM_{array} = True$) and recovering with the higher mode search space enabled ($HM_{search} = True$). These observations were necessary to evaluate the GW data analysis pipeline's performance and understand the signal's properties.

5.3.1 Simulated data

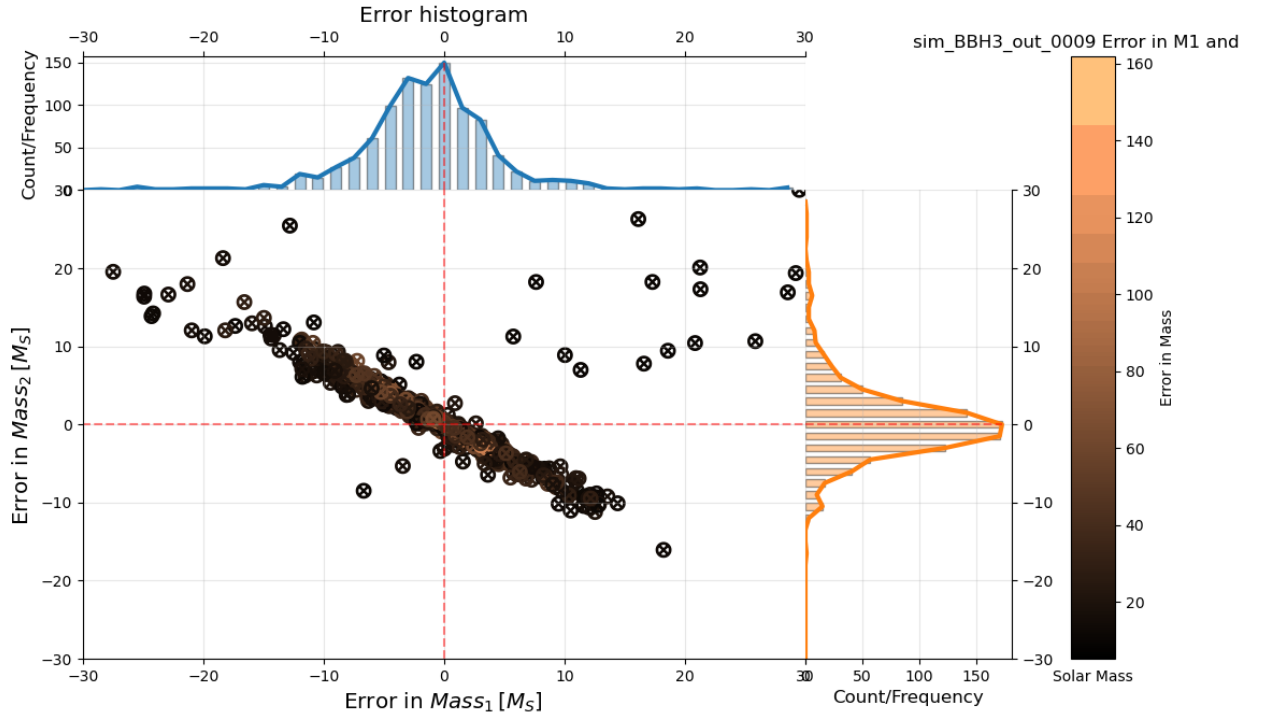
In Fig.5.2a, the points are lying on the diagonal because of the banana-shaped region formed in the M_1/M_2 plane. Here we have injected $60/20M_\odot$ so theoretically, the best match is at $60/20$. However, we find that the same SNR is possible at a range of mass like at $59/21$, $58/22$, and so on. The points not on the diagonals are outliers. The plot is in error in M_1 vs error in M_2 which has some correlation, meaning when ΔM_1 is positive, ΔM_2 should be negative and vice-versa.

In Fig.5.2b, the input vs output plot of chirp mass shows the distribution of the true value of the chirp mass ($\mathcal{M}_{injected}$) and the estimated value of the chirp mass ($\mathcal{M}_{estimated}$) obtained from the PyCBC. Ideally, the plot shows the one-to-one correspondence between the injected and the estimated value. Also, the histogram shows a Gaussian distribution with small standard distribution, indicating the pipeline can accurately estimate the chirp mass. If the histogram showed a large standard deviation or is skewed, it indicates the pipeline was not able to accurately estimate the chirp mass and the estimation is biased.

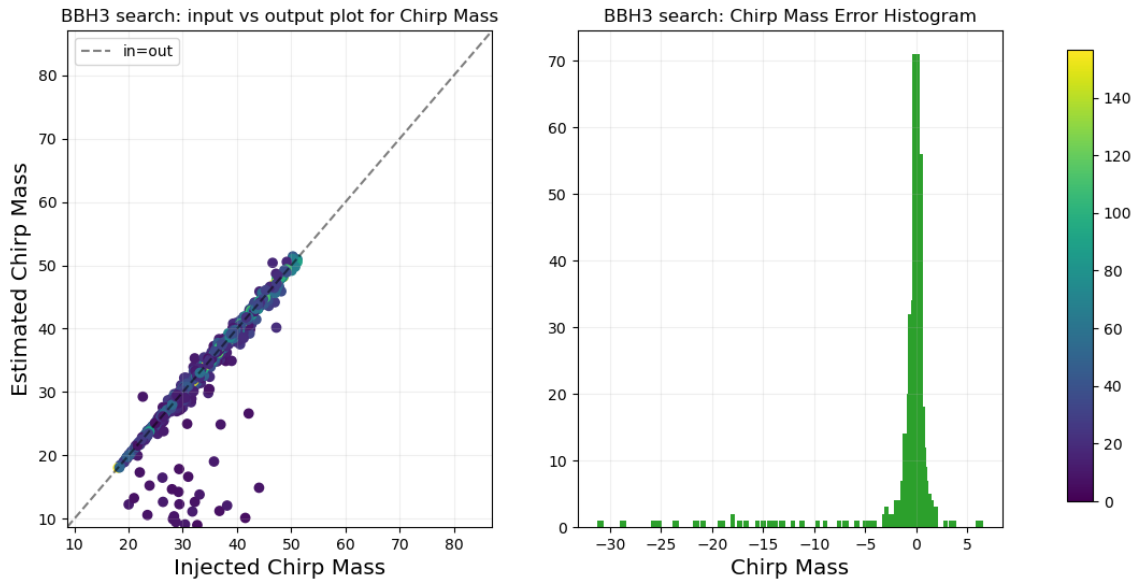
In Fig.5.2c, we see a slight deviation from the one-to-one correspondence between the injected masses and the estimated masses. A little scattering from the $y=x$ line indicates the

pipeline is still able to accurately estimate the masses of black holes, but with some small degree of error. The scatter around the $y=x$ can be quantified by calculating the standard deviation or the root mean square of the error in mass estimation.

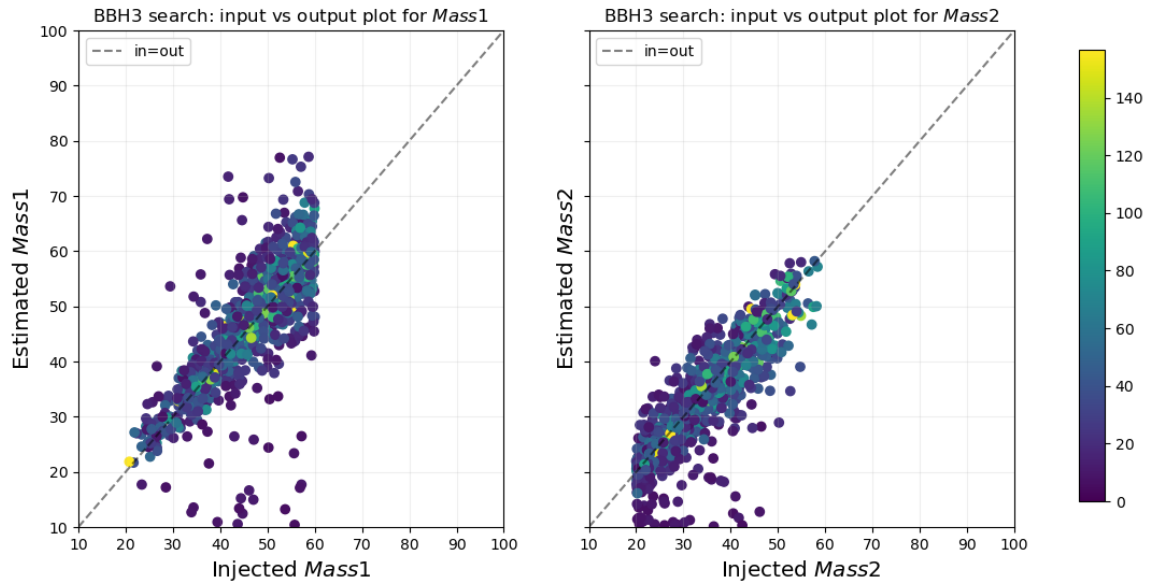
Results when HM search = True, HM array = [2,2]



(A) Error in mass parameters



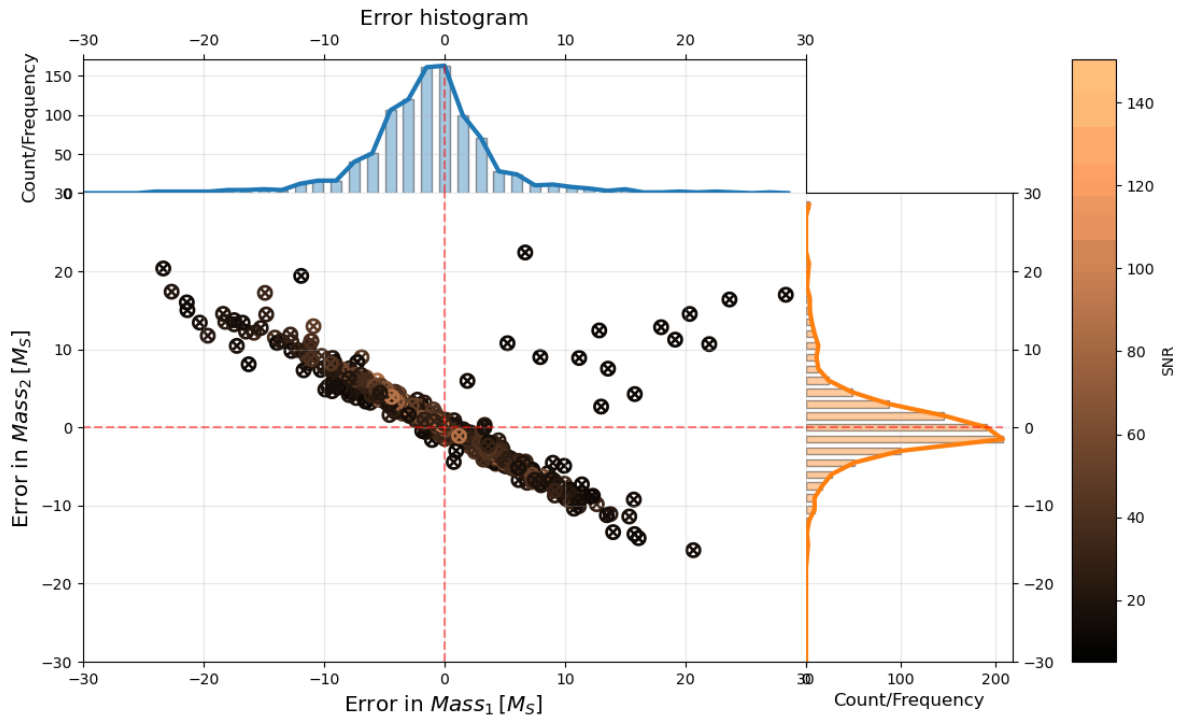
(B) Input vs output plot and error histogram of chirp mass for binary black hole mergers



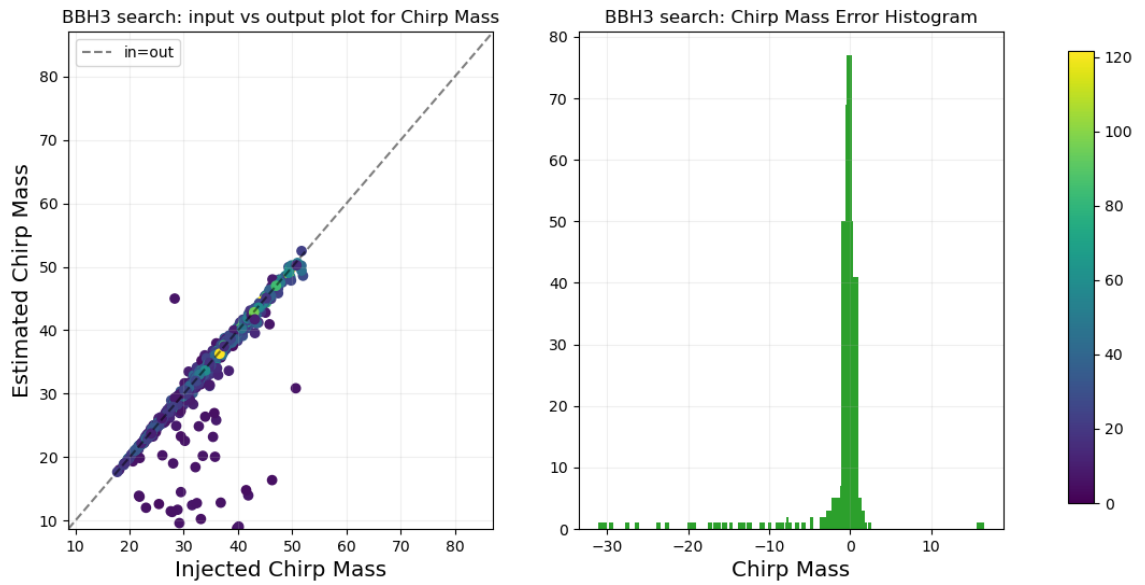
(C) Injected vs estimated masses for binary black hole mergers

FIGURE 5.2: When HM search = True, HM array = [2,2]

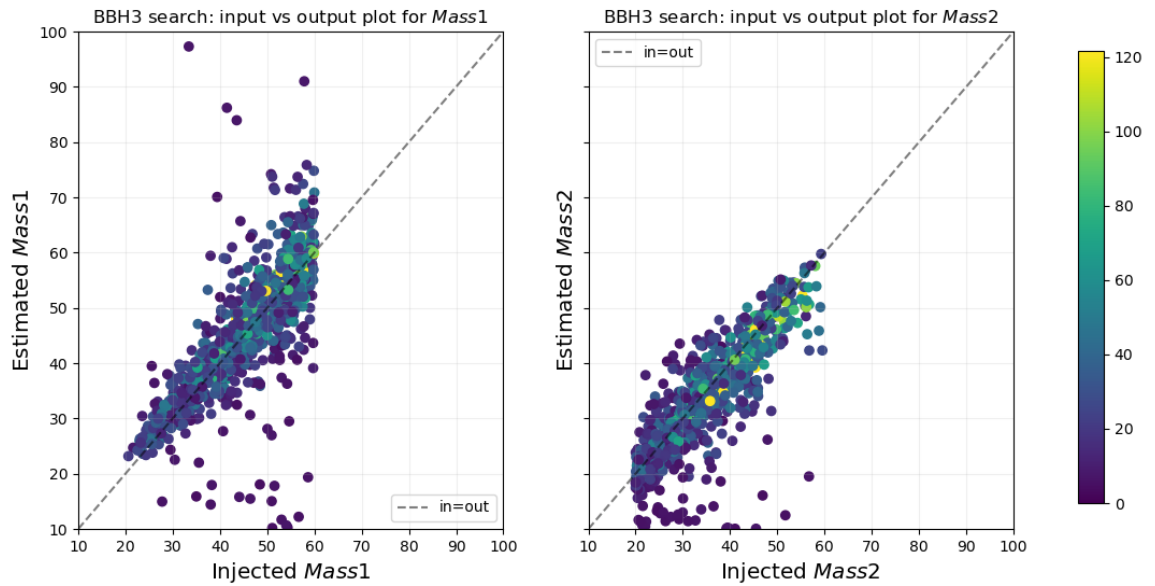
Results when HM search = True, HM array = [2,1], [2,2], [3,3], [4,4]



(A) Error in mass parameters



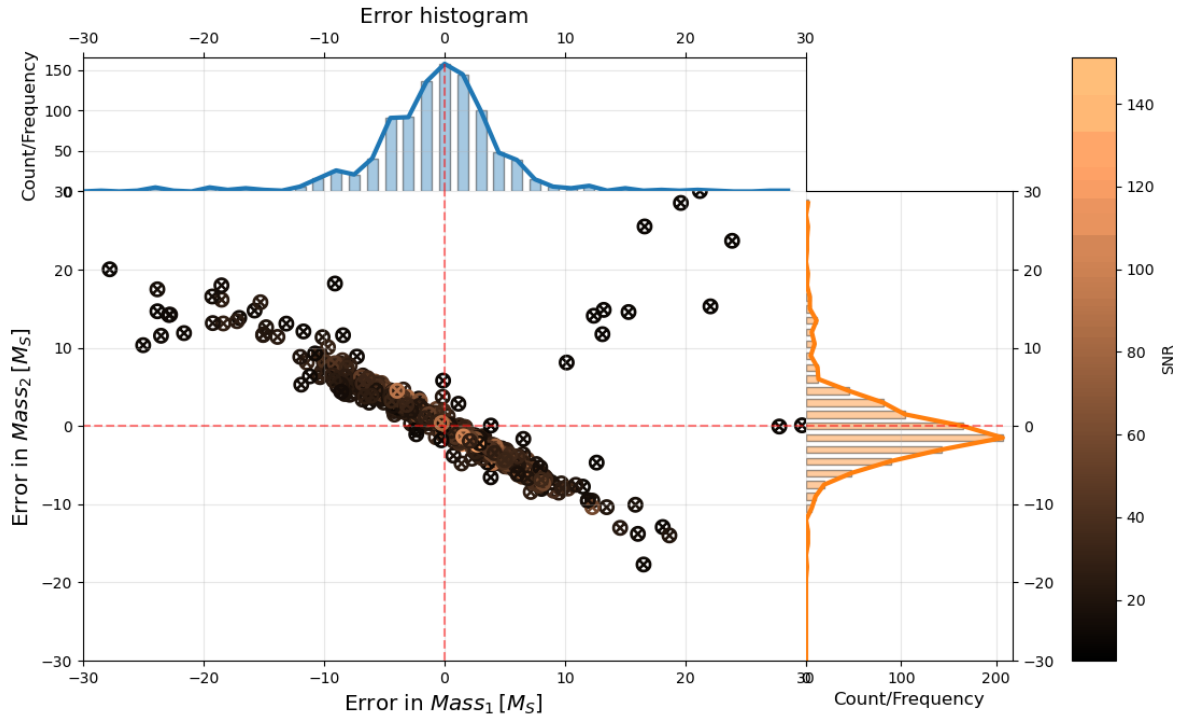
(B) Input vs output plot and error histogram of chirp mass for binary black hole mergers



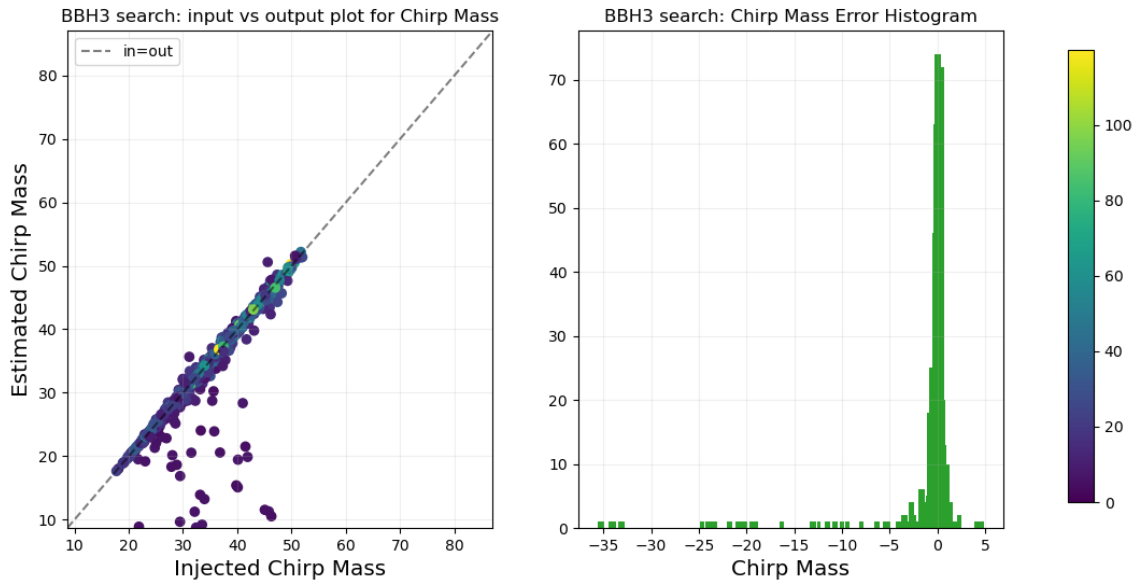
(C) Injected vs estimated masses for binary black hole mergers

FIGURE 5.3: When HM search = True, HM array = [2,1], [2,2], [3,3], [4,4]

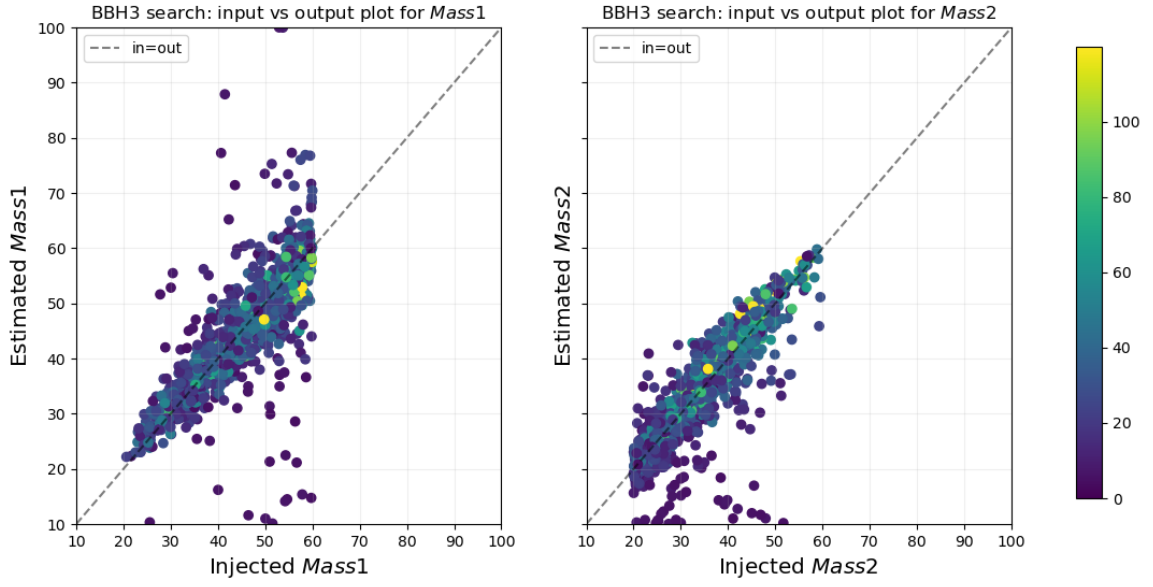
Results when HM array = [2,1], [2,2], [3,3], [4,4] and HM search = False



(A) Error in mass parameters

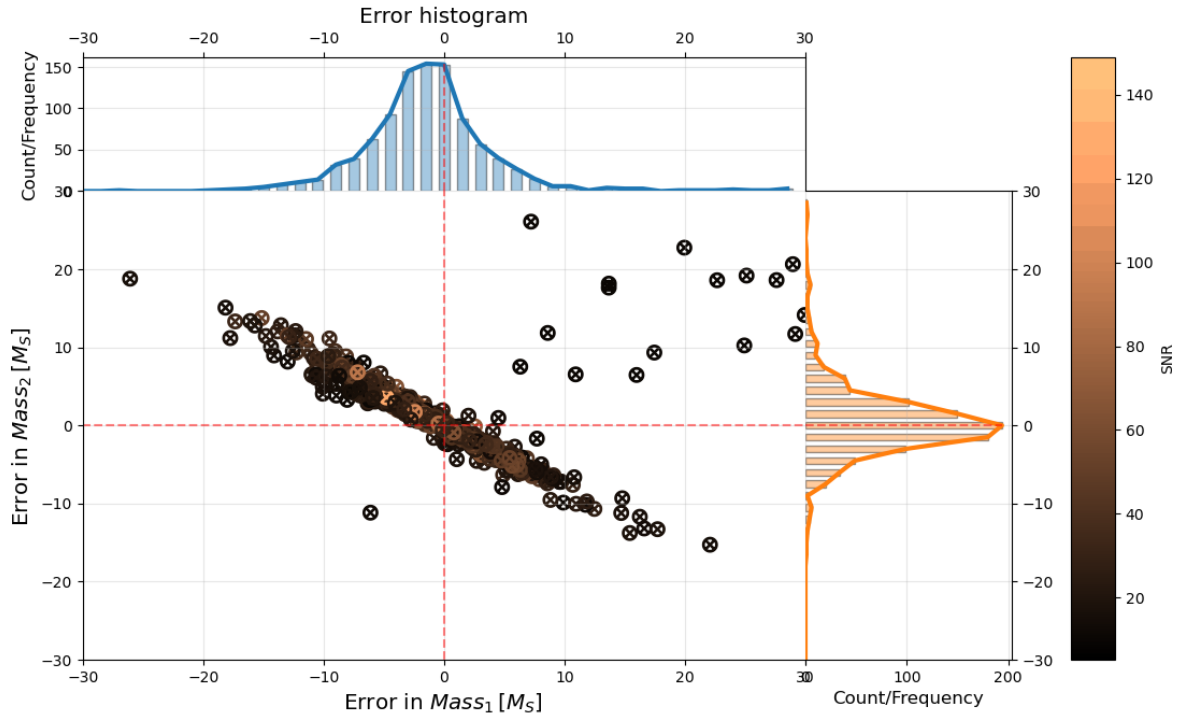


(B) Input vs output plot and error histogram of chirp mass for binary black hole mergers

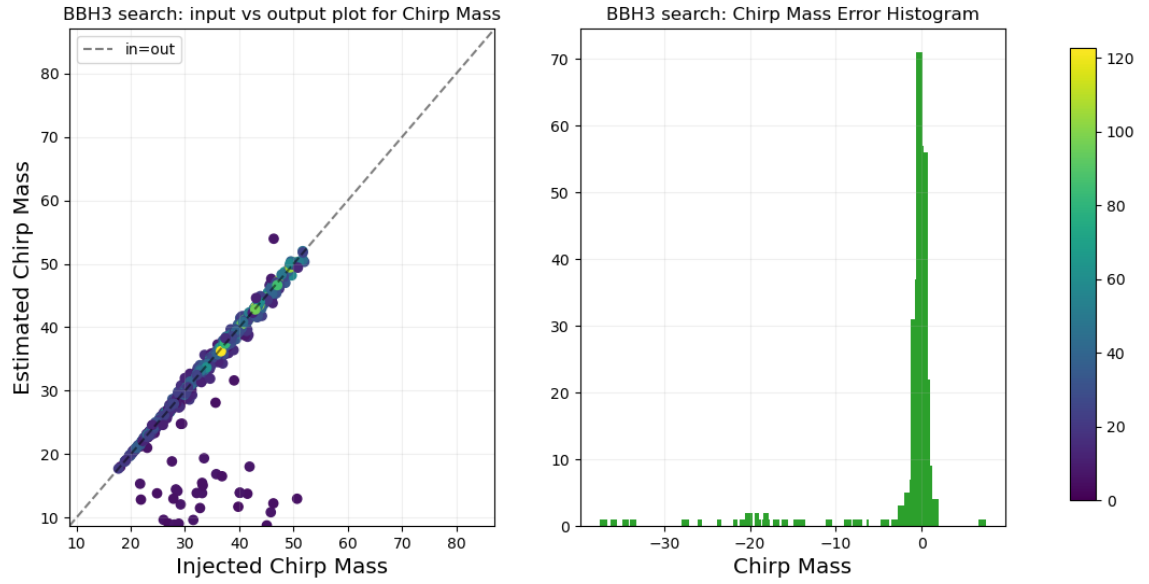


(C) Injected vs estimated masses for binary black hole mergers

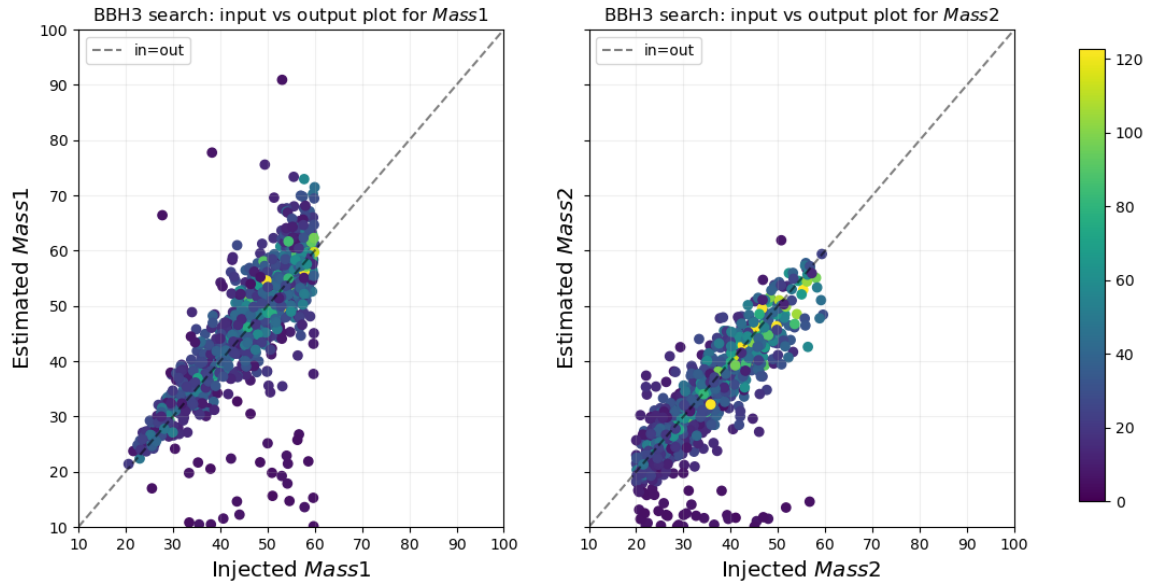
FIGURE 5.4: When HM array = [2,1], [2,2], [3,3], [4,4] and HM search = False

Results when HM array = [2,1], [2,2], [3,3], [4,4] and HM search = True

(A) Error in mass parameters



(B) Input vs output plot and error histogram of chirp mass for binary black hole mergers

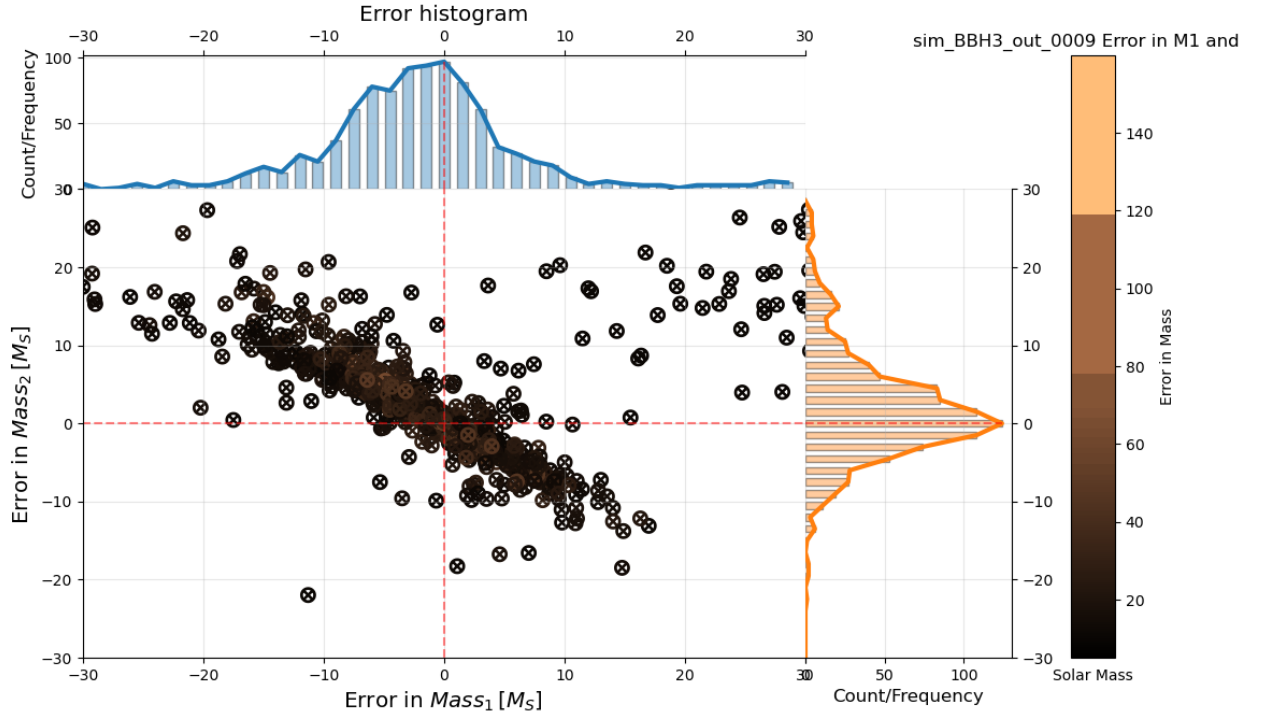


(C) Injected vs estimated masses for binary black hole mergers

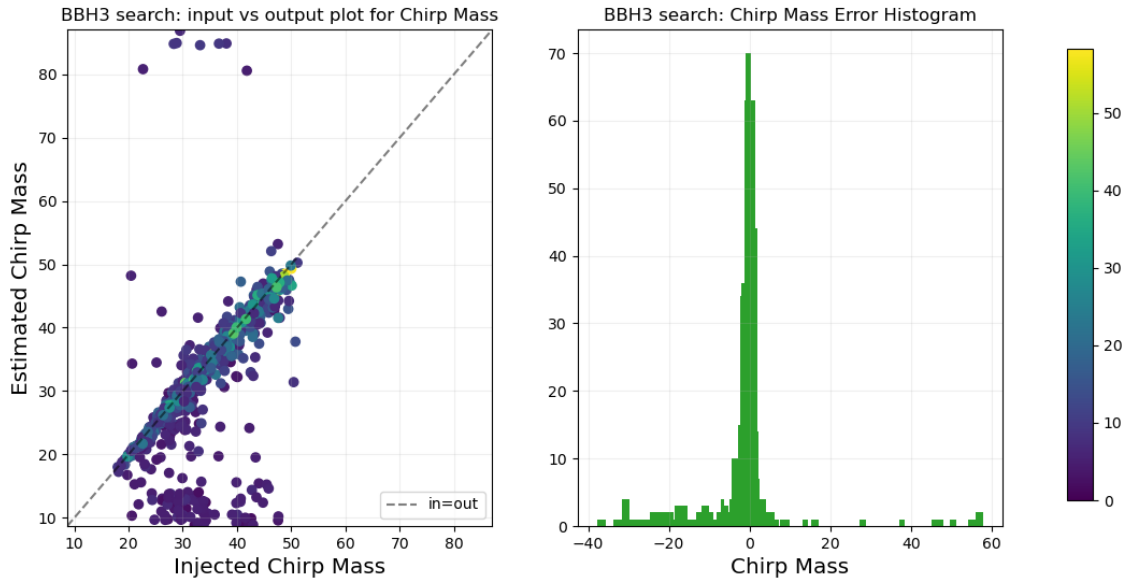
FIGURE 5.5: When HM array = [2,1], [2,2], [3,3], [4,4] and HM search = True

5.3.2 From Astrophysical source

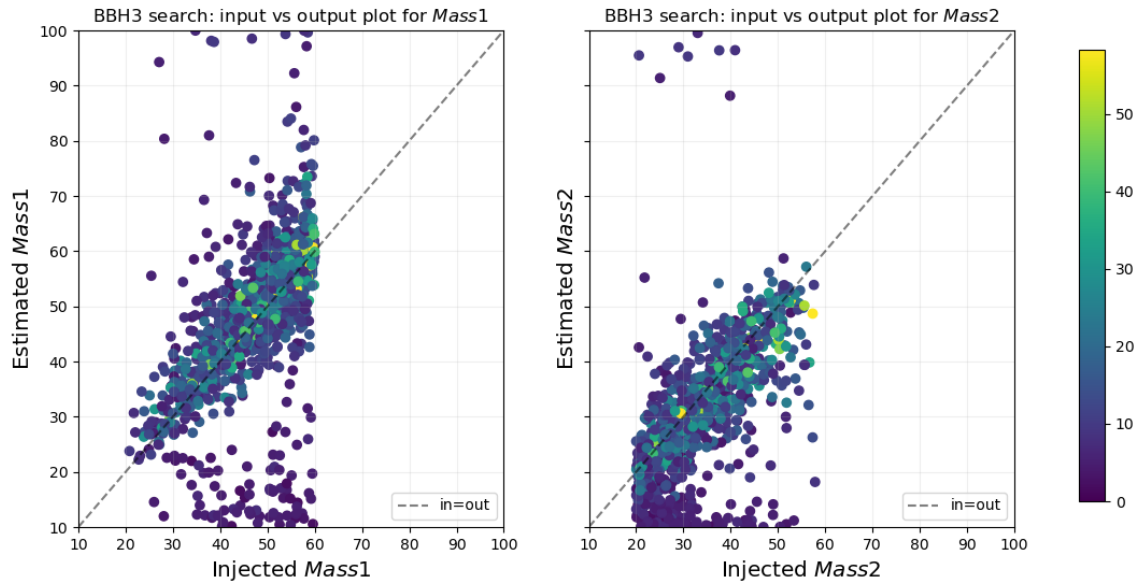
Results when HM search = True, HM array = [2,2]



(A) Error in mass parameters



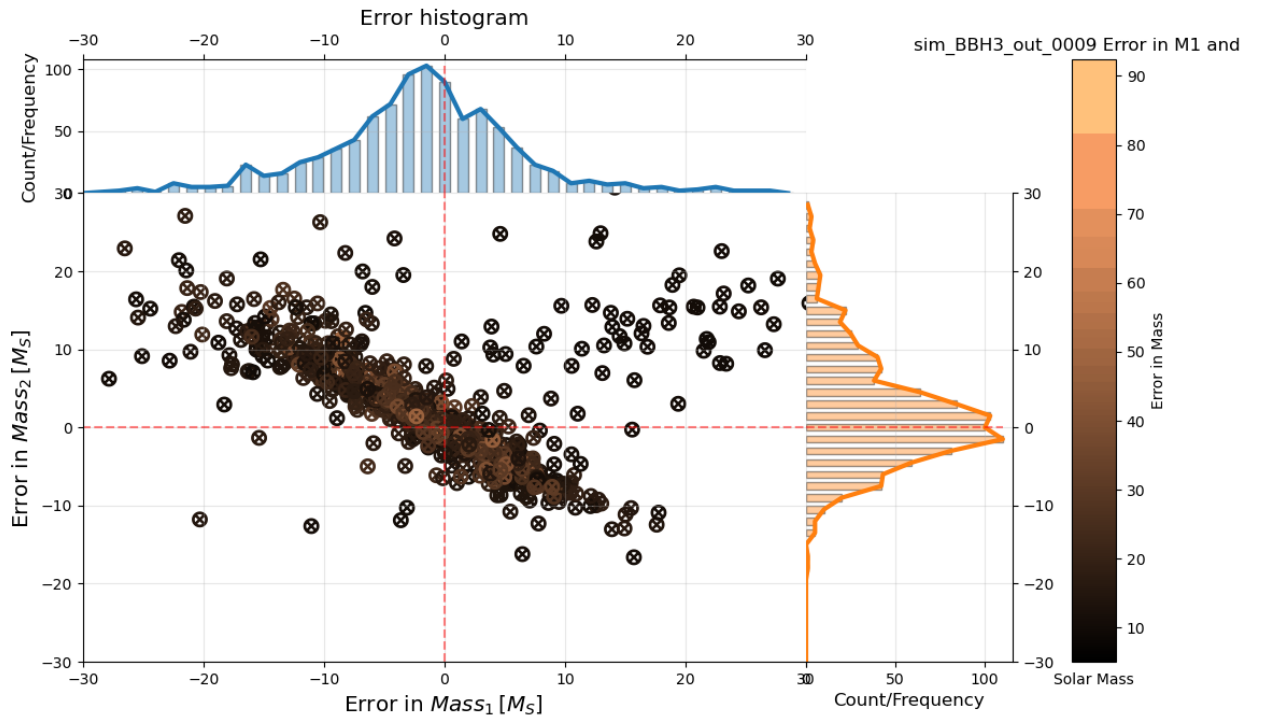
(B) Input vs output plot and error histogram of chirp mass for binary black hole mergers



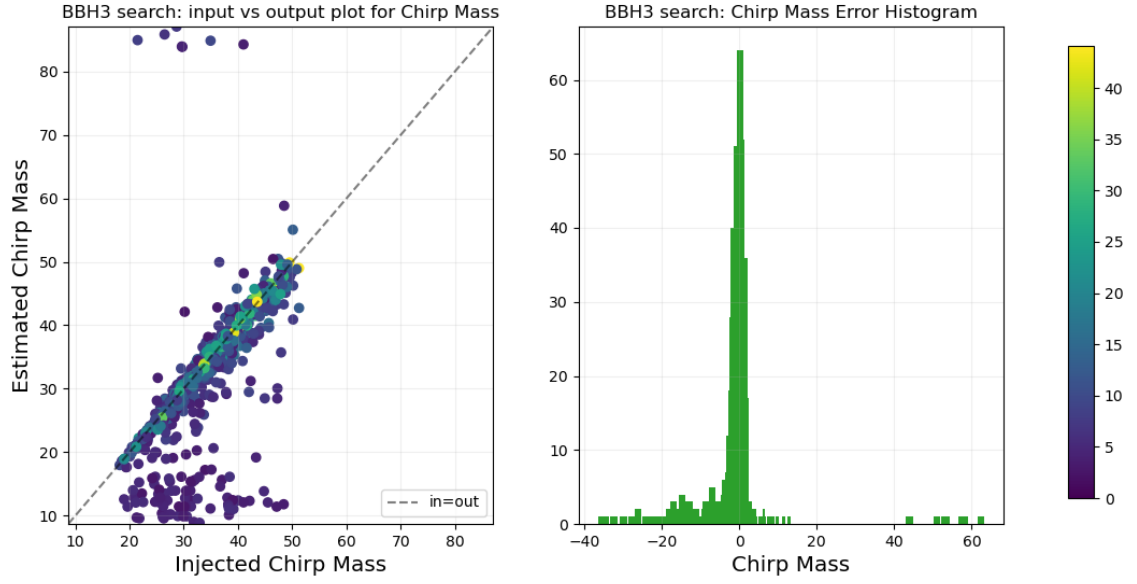
(C) Injected vs estimated masses for binary black hole mergers

FIGURE 5.6: When HM search = True, HM array = [2,2]

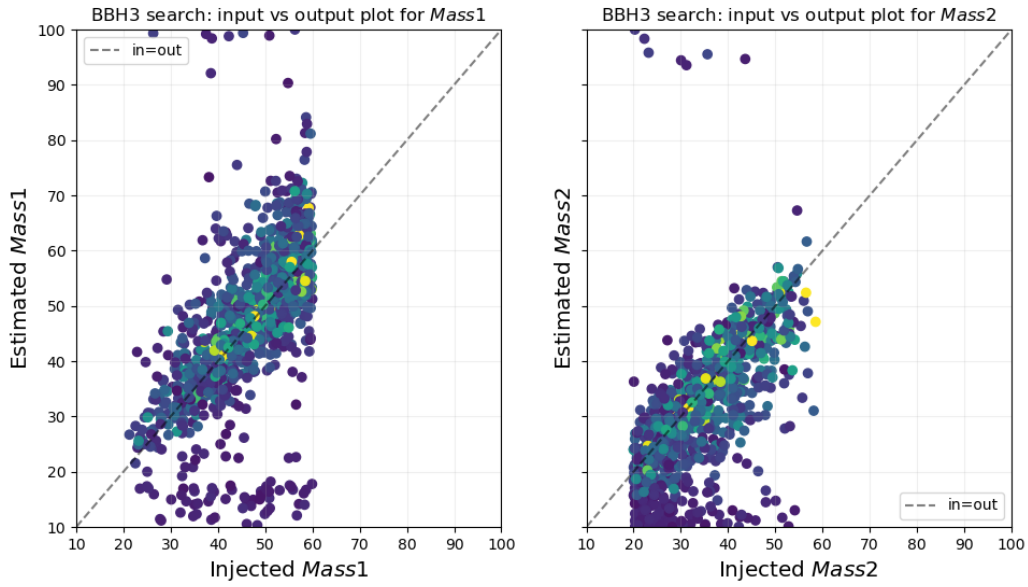
Results when HM search = True, HM array = [2,1], [2,2], [3,3], [4,4]



(A) Error in mass parameters



(B) Input vs output plot and error histogram of chirp mass for binary black hole mergers



(C) Injected vs estimated masses for binary black hole mergers

FIGURE 5.7: When HM search = True, HM array = [2,1], [2,2], [3,3], [4,4]

During the analysis we obtain output files and we mark a significant difference in the SNR values for real events.

| | |
|--|---|
| <pre> 1 { 2 "trig_data": { 3 "1": { 4 "swid": 0, 5 "ifo": "H1", 6 "toa": 1256691943.723877, 7 "snr": 27.162205679575422, 8 "newsnr": 27.162205679575422, 9 "st_time": 1256691936.0, 10 "end_time": 1256691968.0, 11 "gbest": [12 46.96226888861788, 13 28.887310572689884 14] 15 } 16 } 17 }</pre> <p style="text-align: center;">(A)</p> | <pre> 1 { 2 "trig_data": { 3 "1": { 4 "swid": 0, 5 "ifo": "H1", 6 "toa": 1256691942.540039, 7 "snr": 12.285069789644087, 8 "newsnr": 11.968851524909473, 9 "st_time": 1256691936.0, 10 "end_time": 1256691968.0, 11 "gbest": [12 58.867460948904295, 13 26.735802124681143 14] 15 } 16 } 17 }</pre> <p style="text-align: center;">(B)</p> |
|--|---|

FIGURE 5.8: Output files for (A) Simulated event and (B) Real event

In practice, the noise in the data is not perfectly Gaussian, and the amplitude of the noise may vary across the frequency range of the data. This can result in a non-uniform sensitivity of the gravitational wave detector to different frequencies, which can in turn affect the SNR calculation. To account for this non-uniform sensitivity, a process known as re-weighting is often used [38]. Re-weighting involves applying a set of weights to the data before calculating the SNR. The weights are typically chosen to match the sensitivity of the detector at different frequencies to the expected gravitational wave signal. Re-weighting can be particularly important when dealing with real data because the noise in the data can be much more complex and difficult to model accurately than the idealized Gaussian noise used in many theoretical calculations. By re-weighting the data, it is possible to account for these complexities and obtain a more accurate estimate of the SNR.

5.3.3 Chi-squared time-frequency discriminator statistic

Now since we are working on real compact binary coalescence events collected from Gravitational Wave Open Science Center, the sensitivity of the gravitational wave search events gets reduced due to the presence of the non-gaussian noise in the detector data and large SNR can be produced where no signal is present as shown in Fig. 5.9, commonly termed

as *glitches*. These noises often match the template waveforms used in matched filtering, thus match filter method is not sufficient condition to distinguish noise from the astrophysical signals. We implement a machine-learning technique to automatically tune in to the signal-consistency test, called the chi-square test, which works by comparing the PSD of filter output to that of the expected PSD of the Gaussian noise [39].

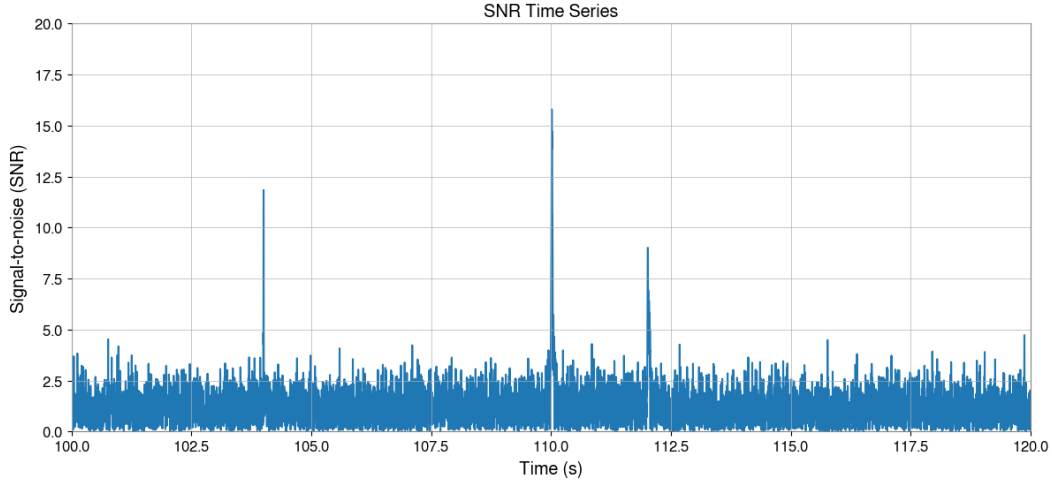


FIGURE 5.9: SNR Time Series plot which contains one signal and two glitches

We see in the SNR time series plot in Fig. 5.9, that there are nice peaks for the frame file we have taken into consideration in the detector. Now we need to test how well the data actually fits model. Analytically, we chop our template into 'p' number of bins and see how much each contributes to the SNR (ρ_i). We then calculate the statistics as the difference between the SNR in one bin, and the fraction of the total SNR (ρ).

$$\chi^2 = \sum_{i=1}^p \left(\frac{\rho_i - \rho}{p} \right)^2 \quad (5.1)$$

We have independent, real and imaginary parts and it has $2p-2$ degrees of freedom. There is also a constraint due to the fact that the sum of each bin must each add up to the total SNR by definition. So we will normalize this statistic by dividing by the number of degrees of freedom, producing χ_r^2 as

$$\chi_r^2 = \frac{p}{2p-2} \sum_{i=1}^p \left(\frac{\rho_i - \rho}{p} \right)^2 \quad (5.2)$$

We expect χ_r^2 to be high when the template does not match with the data, and near unity when the data is either gaussian noise or when it contains the expected signal in addition to the noise. Thus, re-weighting is used in gravitational wave data analysis to account for the non-uniform sensitivity of the detector to different frequencies and to obtain a more accurate estimate of the SNR in the presence of complex, non-Gaussian noise in real data. .

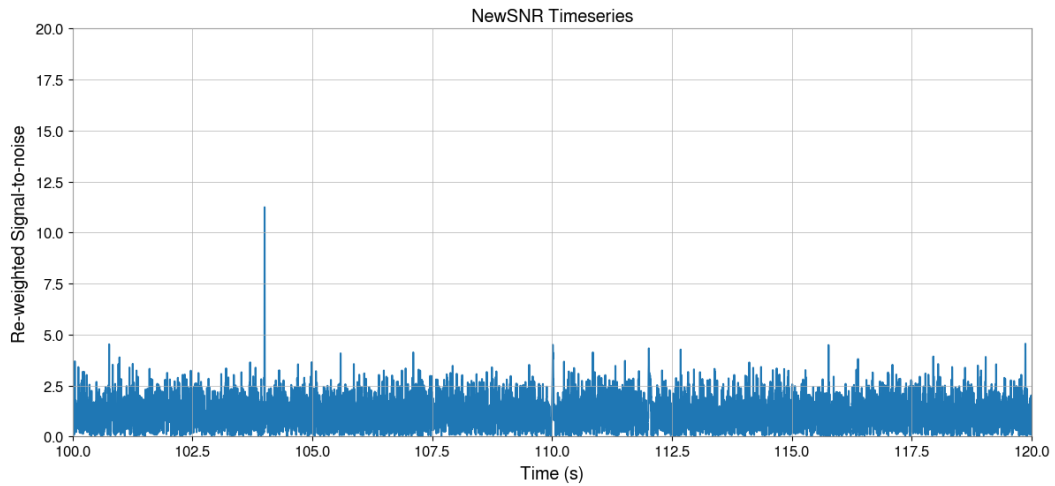


FIGURE 5.10: Re-weighted SNR time series plot, where the SNR peaks at signal

Chapter 6

Conclusion and Future Work

In this dissertation, we have demonstrated for the first time that Artificial intelligence or swarm intelligence can be used for detecting GWs and estimating parameters from GW radiation, even when higher order modes are present. Although the LVK's current algorithms such as matched filtering are optimal to some extent for the detection and parameter estimation of GWs, the number of signals expected to be seen in future observation runs may strain the computational resources required for continued use of such techniques. This thesis presents several unique confirmations-of-principle that demonstrate how effective and efficient AI techniques can be for detecting signals and estimating their parameters.

In Chapter 1, the basic concept of GR and how GWs arises from GR is discussed. The linearized theory of GW is a simplified version of GR that explains how gravitational waves behave in weak gravitational fields. The transverse-traceless gauge, or TT gauge, is a coordinate system that makes it easier to describe GW. It makes sure that the GW is only transverse (perpendicular to the direction of propagation) and traceless (the sum of the diagonal elements of the metric tensor is 0). The Lorenz gauge condition is another mathematical constraint that is used in GR to make sure that the equations that describe how GW works are consistent. It ensures that the divergence of the wave vector is zero. When studying GW with the linearized theory of GR, the TT gauge and Lorenz gauge conditions are used together to make the equations easier to understand and make sure they are mathematically consistent. These conditions are necessary to accurately model how gravitational waves behave and understand their properties, such as their polarisation and amplitude.

In Chapter 2, the standard techniques for GW detection and parameter estimation like match filtering method is discussed. It is shown how the gravitational wave detectors detect GWs, as well as their response based on the location of the source, and the way they account for various noise sources during operation.

In Chapter 3, we discuss one of the artificial intelligence method for detecting GWs which has proved to reduce the false alarm and recovers the different parameters of binary black hole mergers with great accuracy. Since gravitational waveforms from BBH is a fifteen dimensional function, PSO can be used to find optimal solution for such a complex and high-dimensional search space. The algorithm's efficiency, flexibility, robustness, and ease for implementation can speed up the detection process.

In Chapter 4, we see spherical harmonics are used to decompose the GW signal into its constituent modes, which can then be analyzed separately to extract astrophysical information about the source. The modes are characterized by their angular dependence, which is described by the spherical harmonics. The higher-order modes correspond to more complex patterns of spacetime distortion, and they can provide additional information about the source, such as the orientation and spin of the binary system.

In Chapter 5, I present my study in which we used PSO to perform GW detection. We select a gravitational waveform approximant which contains dominant as well as sub-dominant modes. We look for the behaviour of the gravitational wave pipeline when higher modes are enabled (and disabled) for when the simulated data and astrophysical source data are injected into it. We find PSO recovers the SNR accurately even when we have higher harmonics enabled.

Since a single detector is not sufficient to accurately measure the SNR, in the future, we can do a coincident search as a multi-detector network strategy for the real merger events which would take more computing hours than the present one, inject it with the IMRPhe-nomHM waveform approximant, recover with some other approximant containing either dominant mode, sub-dominant mode, or both, and get the SNR for the event. Looking for

higher modes by using PSO in GW data analysis leads to cost reduction, implies lesser time to recover the signal, and we can have a faster prompt system to notify the observatory collaborations across the globe to start looking for EM counterparts from BH-BH mergers or extreme mass ratio NS-BH binaries. With interesting results, the project is in progress, and future work aims to calculate sky localization using PSO.

Bibliography

- [1] Ed Stiles. Researchers at ua and duke university investigate information at the speed of light.
- [2] Frank Watson Dyson, Arthur Stanley Eddington, and Charles Davidson. IX. a determination of the deflection of light by the sun's gravitational field, from observations made at the total eclipse of may 29, 1919. *Philosophical Transactions of the Royal Society of London. Series A, Containing Papers of a Mathematical or Physical Character*, 220(571-581):291–333, 1920.
- [3] Benjamin P Abbott, Richard Abbott, TD Abbott, MR Abernathy, Fausto Acernese, Kendall Ackley, Carl Adams, Thomas Adams, Paolo Addesso, RX Adhikari, et al. Observation of gravitational waves from a binary black hole merger. *Physical review letters*, 116(6):061102, 2016.
- [4] Bernard Schutz. *A first course in general relativity*. Cambridge university press, 2022.
- [5] Benjamin P Abbott, R Abbott, TD Abbott, MR Abernathy, F Acernese, K Ackley, C Adams, T Adams, P Addesso, RX Adhikari, et al. Gw151226: observation of gravitational waves from a 22-solar-mass binary black hole coalescence. *Physical review letters*, 116(24):241103, 2016.
- [6] R Abbott, TD Abbott, S Abraham, F Acernese, K Ackley, A Adams, C Adams, RX Adhikari, VB Adya, Christoph Affeldt, et al. Gwtc-2: compact binary coalescences observed by ligo and virgo during the first half of the third observing run. *Physical Review X*, 11(2):021053, 2021.
- [7] Samantha A Usman, Alexander H Nitz, Ian W Harry, Christopher M Biwer, Duncan A Brown, Miriam Cabero, Collin D Capano, Tito Dal Canton, Thomas Dent, Stephen

- Fairhurst, et al. The pycbc search for gravitational waves from compact binary coalescence. *Classical and Quantum Gravity*, 33(21):215004, 2016.
- [8] BP Abbott, Richard Abbott, TDea Abbott, S Abraham, F Acernese, K Ackley, C Adams, RX Adhikari, VB Adya, Christoph Affeldt, et al. Gwtc-1: a gravitational-wave transient catalog of compact binary mergers observed by ligo and virgo during the first and second observing runs. *Physical Review X*, 9(3):031040, 2019.
- [9] Benjamin P Abbott, Robert Abbott, TD Abbott, F Acernese, K Ackley, C Adams, T Adams, P Addresso, RX Adhikari, VB Adya, et al. Gravitational waves and gamma-rays from a binary neutron star merger: Gw170817 and grb 170817a. *The Astrophysical Journal Letters*, 848(2):L13, 2017.
- [10] R Abbott, TD Abbott, S Abraham, F Acernese, K Ackley, A Adams, C Adams, RX Adhikari, VB Adya, Christoph Affeldt, et al. Observation of gravitational waves from two neutron star–black hole coalescences. *The Astrophysical journal letters*, 915(1):L5, 2021.
- [11] John Antoniadis, Thomas M Tauris, Feryal Ozel, Ewan Barr, David J Champion, and Paulo CC Freire. The millisecond pulsar mass distribution: Evidence for bimodality and constraints on the maximum neutron star mass. *arXiv preprint arXiv:1605.01665*, 2016.
- [12] Russell A Hulse and Joseph H Taylor. Discovery of a pulsar in a binary system. *The Astrophysical Journal*, 195:L51–L53, 1975.
- [13] Joel M Weisberg and Joseph H Taylor. Relativistic binary pulsar b1913+ 16: Thirty years of observations and analysis. *arXiv preprint astro-ph/0407149*, 2004.
- [14] Junaid Aasi, BP Abbott, Richard Abbott, Thomas Abbott, MR Abernathy, Kendall Ackley, Carl Adams, Thomas Adams, Paolo Addresso, RX Adhikari, et al. Advanced ligo. *Classical and quantum gravity*, 32(7):074001, 2015.
- [15] Fet al Acernese, M Agathos, K Agatsuma, D Aisa, N Allemandou, A Allocca, J Amarni, P Astone, G Balestri, G Ballardin, et al. Advanced virgo: a second-generation interferometric gravitational wave detector. *Classical and Quantum Gravity*, 32(2):024001, 2014.

- [16] C Affeldt, K Danzmann, KL Dooley, H Grote, M Hewitson, S Hild, J Hough, J Leong, H Lück, M Prijatelj, et al. Advanced techniques in geo 600. *Classical and quantum gravity*, 31(22):224002, 2014.
- [17] Kagra: 2.5 generation interferometric gravitational wave detector. *Nature Astronomy*, 3(1):35–40, 2019.
- [18] Pau Amaro-Seoane, Sofiane Aoudia, Stanislav Babak, Pierre Binetruy, Emanuele Berti, Alejandro Bohé, Chiara Caprini, Monica Colpi, Neil J Cornish, Karsten Danzmann, et al. elisa: Astrophysics and cosmology in the millihertz regime. *arXiv preprint arXiv:1201.3621*, 2012.
- [19] Jun Luo, Li-Sheng Chen, Hui-Zong Duan, Yun-Gui Gong, Shoucun Hu, Jianghui Ji, Qi Liu, Jianwei Mei, Vadim Milyukov, Mikhail Sazhin, et al. Tianqin: a space-borne gravitational wave detector. *Classical and Quantum Gravity*, 33(3):035010, 2016.
- [20] Albert A Michelson and Edward W Morley. Lviii. on the relative motion of the earth and the luminiferous æther. *The London, Edinburgh, and Dublin Philosophical Magazine and Journal of Science*, 24(151):449–463, 1887.
- [21] Alfred Perot and Charles Fabry. On the application of interference phenomena to the solution of various problems of spectroscopy and metrology. *Astrophysical Journal*, vol. 9, p. 87, 9:87, 1899.
- [22] Warren G Anderson, Patrick R Brady, Jolien DE Creighton, and Eanna E Flanagan. Excess power statistic for detection of burst sources of gravitational radiation. *Physical Review D*, 63(4):042003, 2001.
- [23] Samantha A Usman, Alexander H Nitz, Ian W Harry, Christopher M Biwer, Duncan A Brown, Miriam Cabero, Collin D Capano, Tito Dal Canton, Thomas Dent, Stephen Fairhurst, et al. The pycbc search for gravitational waves from compact binary coalescence. *Classical and Quantum Gravity*, 33(21):215004, 2016.
- [24] Christopher Michael Biwer, Collin D Capano, Soumi De, Miriam Cabero, Duncan A Brown, Alexander H Nitz, and Vivien Raymond. Pycbc inference: A python-based parameter estimation toolkit for compact binary coalescence signals. *Publications of the Astronomical Society of the Pacific*, 131(996):024503, 2019.

-
- [25] P Ajith, Satya Mohapatra, and Archana Pai. A gravitational-wave data analysis primer for the indigo mock data challenge. *Neutron stars*, 1:1–5.
- [26] Michele Maggiore. *Gravitational waves: Volume 1: Theory and experiments*. OUP Oxford, 2007.
- [27] J. Kennedy and R. Eberhart. Particle swarm optimization. In *Proceedings of ICNN'95 - International Conference on Neural Networks*, volume 4, pages 1942–1948 vol.4, 1995.
- [28] Abha Singh, Abhishek Sharma, Shailendra Rajput, Amarnath Bose, and Xinghao Hu. An investigation on hybrid particle swarm optimization algorithms for parameter optimization of pv cells. *Electronics*, 11(6):909, 2022.
- [29] Michele Maggiore. *Gravitational Waves: Volume 2: Astrophysics and Cosmology*. Oxford University Press, 2018.
- [30] Chinmay Kalaghatgi, Mark Hannam, and Vivien Raymond. Parameter estimation with a spinning multimode waveform model. *Phys. Rev. D*, 101:103004, May 2020.
- [31] Katerina Chatziioannou, Roberto Cotesta, Sudarshan Ghonge, Jacob Lange, Ken KY Ng, Juan Calderón Bustillo, James Clark, Carl-Johan Haster, Sebastian Khan, Michael Pürrer, et al. On the properties of the massive binary black hole merger gw170729. *Physical Review D*, 100(10):104015, 2019.
- [32] Yan Wang and Soumya D Mohanty. Particle swarm optimization and gravitational wave data analysis: Performance on a binary inspiral testbed. *Physical Review D*, 81(6):063002, 2010.
- [33] Varun Srivastava, K Rajesh Nayak, and Sukanta Bose. Toward low-latency coincident precessing and coherent aligned-spin gravitational-wave searches of compact binary coalescences with particle swarm optimization. *arXiv preprint arXiv:1811.02401*, 2018.
- [34] R Abbott, H Abe, F Acernese, K Ackley, S Adhicary, N Adhikari, RX Adhikari, VK Adkins, VB Adya, C Affeldt, et al. Open data from the third observing run of ligo, virgo, kagra and geo. *arXiv preprint arXiv:2302.03676*, 2023.

-
- [35] Ethan Payne, Colm Talbot, and Eric Thrane. Higher order gravitational-wave modes with likelihood reweighting. *Physical Review D*, 100(12):123017, 2019.
- [36] Shasvath J Kapadia, Mukesh Kumar Singh, Md Arif Shaikh, Deep Chatterjee, and Parameswaran Ajith. Of harbingers and higher modes: improved gravitational-wave early warning of compact binary mergers. *The Astrophysical Journal Letters*, 898(2):L39, 2020.
- [37] Mukesh Kumar Singh, Shasvath J Kapadia, Md Arif Shaikh, and Parameswaran Ajith. Improved early-warning estimates of luminosity distance and orbital inclination of compact binary mergers using higher modes of gravitational radiation. *Monthly Notices of the Royal Astronomical Society*, 513(3):3798–3809, 2022.
- [38] Connor McIsaac and Ian Harry. Using machine learning to autotune chi-squared tests for gravitational wave searches. *Physical Review D*, 105(10):104056, 2022.
- [39] Alexander H Nitz. Distinguishing short duration noise transients in ligo data to improve the pycbc search for gravitational waves from high mass binary black hole mergers. *Classical and Quantum Gravity*, 35(3):035016, 2018.